Applied Catalysis B: Environmental 298 (2021) 120614

Contents lists available at ScienceDirect

Applied Catalysis B: Environmental

journal homepage: www.elsevier.com/locate/apcatb

Plasmon activation *versus* plasmon quenching on the overall photocatalytic performance of Ag/Au bimetal decorated g-C_3N_4 nanosheets under selective photoexcitation: A mechanistic understanding with experiment and theory

Trishamoni Kashyap [a,b], Sritam Biswas [c], Shahnaz Ahmed [d], Dhrubajyoti Kalita [d], Pabitra Nath [c], Biswajit Choudhury [a,*]

[a] Materials and Energy Laboratory, Physical Sciences Division, Institute of Advanced Study in Science and Technology, Paschim Boragaon, Guwahati 35, Assam, India
[b] Departmentof Physics, Cotton University, Panbazar, Guwahati 01, Assam, India
[c] Department of Physics, Tezpur University, Napaam 784028, Assam, India
[d] Department of Chemistry, Gauhati University, Guwahati 781014, Assam, India

ARTICLE INFO

Keywords:
Plasmonic
Interband transition
Defects
FRET
PIRET
Photocatalysis

ABSTRACT

The exploitation of surface plasmon resonance (SPR) properties of metal nanoparticles (NPs) are considered beneficial for an improved photocatalysis under visible and near infra-red (NIR) photons. Here, on the contrary, we have shown a retarding plasmonic activity in Ag/Au bimetals decorated g-C_3N_4 nanosheets in rhodamine B (RhB) degradation under UV–vis and green laser. It is argued that Förster-resonance energy transfer (FRET) and plasmon-induced resonance energy transfer (PIRET) counteract with each other on illuminations. The experimental findings, electromagnetic simulation, and density-functional theory (DFT) results infer that reduced optical field intensity at the bimetallic gap, dominance of FRET over PIRET, nearest metal Fermi surface with semiconductor holes, and interfacial trap centers are possibly contributing to a quenched plasmonic photocatalysis. It is further stated that the semiconductor excitation and interband *d-sp* induced hot electrons over the bimetals are favoring an enhanced photocatalysis under UV light.

1. Introduction

Semiconductor TiO_2 based photocatalytic water splitting started three decades back with the remarkable Honda-Fujishima effect [1]. However, TiO_2 being a wide bandgap (3.2 eV) semiconductor, is inefficient to harvest visible to near infra-red light (NIR). Doping of ions, composites, defect engineering, and surface functionalization are strategies that can improve efficiency [2]. Dopants and defects introduce mid-band gap states and enhance visible light absorption. Composite heterostructures achieve better interfacial charge separation and light absorption [2–6]. Many of the published results reveal that fiber-based hybrid nanomaterials show excellent photocatalytic activities under visible light. For example, a flexible carbon fibre (CF) based TiO_2/A-g_2O/CF photocatalyst with broad absorption range (200−1000 nm) and interfacial charge separation effectively degrade (>90 %) organic dyes under visible and NIR illumination [4]. AgBr/Ag_3PO_4 heterostructure loaded on chitosan fibres (CTF) with numerous active sites and large interfacial contact area degrades methyl orange (MO) under visible light [5]. Rhodizonic acid-functionalized TiO_2 nanofibre shows a much faster degradation of methylene blue (MB) than unmodified TiO_2 nanofibre under visible light [6]. Despite the surface modifications, TiO_2 based photocatalyst still suffers from poor dispersion in water, which also affects its long-term activity. In 2009, the discovery of metal-free g-C_3N_4 photocatalyst had been considered the newest addition in heterogeneous photocatalysis [7]. In its pristine form, g-C_3N_4 suffers from fast carrier recombination and poor photoconversion efficiency in the green and red regions of the solar spectrum [8]. Strategies such as composite with semiconductors, conjugation with organic polymers, and metal decoration were expected to improve the photocatalytic performance of g-C_3N_4 [8–14]. For example, g-C_3N_4 nanosheets synthesized using the supramolecular chemistry approach show enhanced light absorption and efficient H_2 production under solar light [11]. Lignin modified

* Corresponding author.
E-mail address: biswajitchoudhury@iasst.gov.in (B. Choudhury).

https://doi.org/10.1016/j.apcatb.2021.120614
Received 30 April 2021; Received in revised form 20 July 2021; Accepted 9 August 2021
Available online 11 August 2021

g-C_3N_4 nanostructure with ideal band structure and extended visible light absorption produces a 3.5 times higher rate of H_2 evolution than its pristine counterpart [12]. A Z-scheme system of Ag_3PO_4/g-C_3N_4 with long-lived photogenerated holes shows efficient oxygen evolution performance under LED irradiation [13]. 2D/2D assembly of protonated g-C_3N_4/Ti_3C_2 MXene exhibits facile interfacial charge transport and excellent H_2 production than its pristine counterparts [14].

In recent years, SPR properties of metal NPs are exploited to maximize the photoconversion efficiency of g-C_3N_4 under broad-band solar light. The available literature shows that Ag and Au NPs clubbed with g-C_3N_4 show a much-improved photocatalytic H_2 production and organic pollutant degradation [15–20]. However, compared to single metal decoration, bimetallic combinations of Au/Pd, Ag/Pd, and Ag/Au decorated over g-C_3N_4, reportedly show enhanced photocatalytic dye degradation and H_2 production under visible light [21–25]. As reported, the benefits of bimetals in photocatalysis are: SPR mediated visible-light absorption covering an extended visible range, metal-to-metal and metal-semiconductor supported interaction, and charge separation. A few studies also report reduced photocatalysis with bimetallic composites [26–28].

Herein, we have reported the photocatalytic activity of Ag/Au-g-C_3N_4 under UV, UV–vis, and green laser illumination. The motivations behind fabricating Ag/Au-g-C_3N_4 for photocatalysis are described point wise. First, the mean free path (λ_{mp}) of electrons in Ag is 53.3 nm, and 37.7 nm in silver [29]. Thus, the SPR promoted electrons with longer λ_{mp} swiftly move from bulk to the surface of Ag/Au bimetals for participating in photocatalysis. Second, instead of a constraint SPR absorption corresponding to individual Ag (~425 nm) and Au (~526 nm) [15], the introduction of bimetals could promote tunable light absorption in the ~400−600 nm window. Third, by using UV light, the interband absorption of Ag and Au can be exploited for carrier generation, thus achieving enhanced photocatalysis [30]. However, contrary to our presumption, the bimetals have not shown satisfactory results in photocatalytic RhB degradation. This study, therefore, analyzes the reduced photocatalytic performance of Ag/Au-g-C_3N_4 with experiment and theory. Some of the initial experiments and theoretical studies helped us determine the reasons for the quenched plasmonic photocatalysis. The points of interest of the present study are highlighted here. First, band structure determination with ultraviolet photoelectron spectroscopy (UPS) and DFT reveals that the Ag/Au Fermi surface (E_f) is near the valence band (VB) of g-C_3N_4, thus, imposing the possibility of facile recombination of Fermi surface electrons with VB holes in g-C_3N_4. Second, electromagnetic (EM) field simulation shows reduced localized electric field intensity at the Ag-Au bimetallic separation under monochromatic visible excitation. It, thus, indicates damping of plasmon energy in bimetal combination. Third, the oxidized Au^+ and Ag^+ species in the composite act as interfacial electron traps and dampen the plasmonic field. Fourth, both EM simulation and photoconductivity measurement show hot carrier generation under UV and visible (420 nm) excitation through interband and plasmon excitation. Further, the roles of PIRET and FRET on photocatalysis are discussed [31]. The best photocatalytic result for the bimetallic composite is recorded under UV light. UV illumination enables interband *d-sp* transition and produces enough carriers over the metal surface for triggering photocatalysis. Further, we have expanded our understanding of photocatalysis with other organic contaminants, such as methylene blue (MB), methyl orange (MO), and phenol. The comparison shows that pristine and bimetallic composites show relatively poor MB, MO, and phenol degradation under a similar experimental set-up. Of all the bimetallic composites, on average, Ag0.1Au0.9CN shows better photocatalytic performance under selective excitations. Therefore, we find that parameters such as Ag/Au composition, incident radiation, plasmon-semiconductor absorption edge, and finally, the nature of dye affect the photocatalytic performance of the bimetallic composites.

2. Experimental details

2.1. Chemicals

Urea is purchased from Merck, India. Gold chloride trihydrate ($HAuCl_4.3H_2O$), silver nitrate ($AgNO_3$), and the model pollutants RhB, MB, MO, and phenol are purchased from Sigma Aldrich (India) and Merck (India). The solvents acetone and propanol are purchased from Merck (India). The other chemicals are di-potassium oxalate monohydrate ($K_2C_2O_4.H_2O$, Merck, India), *tert*-butanol ($C_4H_{10}O$, Merck India), p-benzoquinone ($C_6H_4O_2$, Sigma Aldrich), and carbon tetrachloride (CCl_4, Loba Chemie Pvt. Ltd.).

2.2. Synthesis of photocatalysts

Pristine g-C_3N_4 (CN) is prepared by heating urea in a furnace at 550 °C for 3 h. The final product is lightweight, powdery, and pale-yellow colored. The following procedure is employed for the synthesis of bimetallic nanocomposites. Typically, gold (III) chloride trihydrate is dissolved in 100 mL ultrapure water to make 'X' mM gold chloride solution. First, the solution is heated to boiling. To the boiled solution, 30 mM trisodium citrate (TSC) solution is added drop-wise. The change in color from pale yellow to dark wine-red indicates the formation of Au NPs. Next, 'Y' mM silver nitrate solution is prepared by adding $AgNO_3$ in 100 mL water. The $AgNO_3$ solution is added to an already prepared Au NPs solution and stirred well. The mixture is heated to 100 °C, and TSC solution is added drop-wise. For the bimetallic composite preparation, CN (200 mg) is added to the boiling mixture and stirred for another 30 min. The final product (AgYAuXCN) is collected by washing followed by drying in an oven. Here, X and Y are 0.1 mM, 0.3 mM, 0.5 mM, 0.7 mM, and 0.9 mM, respectively. The prepared catalysts are named CXY, where X, Y are the concentration of gold and silver precursors, respectively. The renaming of the samples are as follows: Ag0.1Au0.9CN (C91), Ag0.3Au0.7CN (C73), Ag0.5Au0.5CN (C55), Ag0.7Au0.3 (C37), and Ag0.9Au0.1 (C19).

2.3. Characterization

The crystalline structure of the prepared photocatalysts is obtained under a Cu *kα* X-ray beam of $\lambda = 0.154$ nm (Bruker D8 Advance X-ray diffractometer). The different optical transitions are recorded in a diffuse-reflectance (DR) mode (Shimadzu UV-2600 spectrophotometer). Photoluminescence (PL) spectra are monitored with a Fluromax-4 spectrometer (Horiba Scientific). Time-dependent PL intensity decay is observed with a picoseconds time-resolved fluorescence spectrometer (Edinburg Instruments, FSP920). The samples' morphology is viewed with a high-resolution transmission electron microscope (200 kV HRTEM, JEOL Ltd.). Energy-dispersive X-ray (EDX) spectroscopy of pristine and photocatalytically recycled samples are taken in JSM 6390 L V scanning electron microscope (SEM, JEOL). Core-level and valence band (VB) X-ray photoelectron spectra (XPS) are acquired in an ESCALAB Xi+ (Thermo Fischer Scientific Pvt. Ltd., UK) with Au as the reference. Al kα is taken as the X-ray source of exciting energy 1486 eV with 50 eV as the pass energy for individual element scanning. Ultraviolet photoelectron spectroscopy (UPS) data are collected by exciting the samples with energy of 22.21 eV (He-I).

2.4. Photocatalytic experiment

The bimetallic composite's catalytic performance is investigated from RhB degradation under UV, UV–vis, and green laser irradiation. 40 mg of the catalyst is added to 200 mL of RhB solution with an initial dye concentration of 10 mg L^{-1}. The mixture is stirred for 45 min under dark to ensure better interfacial contact between the catalyst and dye solution. The solutions are irradiated with UV and UV–vis lamps of 250 W for 105 min. Nearly 5 mL of aliquot is collected after 15 min, and the

degradation is measured by monitoring the decrease in absorption intensity of RhB.

For the photocatalytic reaction under a green laser (532 nm), the dye solution is diluted to make an initial concentration of 2.5 mg L^{-1} in 50 mL water. The catalyst amount is proportionately reduced to 10 mg. The beaker is covered up with aluminium foil, leaving an aperture as a provision for laser illumination. The dye-catalyst solution is constantly stirred for 45 min under dark as before. After each 15 min, 2 mL solution is collected, and absorption is measured with a UV–vis spectrophotometer. The same procedure is adopted to study degradation of MO, MB, and phenol under selective excitation ranges (UV, UV–vis, and green laser).

We have tested the heterogeneity and reusability of the bimetallic catalyst by conducting a leaching experiment. The catalyst C73 (10 mg) is taken in 50 mL water containing an initial dye concentration of 2.5 mg L^{-1}. The photocatalytic experiment is similar to that reported for the green laser. The photocatalytic reaction is continued for 3 consecutive cycles, with each cycle performed for 105 min. After each cycle, the catalyst is recovered, washed thoroughly, dried at 70 °C, and poured into another freshly prepared dye solution for performing the 2nd cycle, and so on. We have taken EDX and XRD to see the surface composition of leached samples and the stability of the photocatalyst, respectively.

Different sacrificial reagents are used to identify the radical species that accelerates the photocatalytic degradation of RhB. di-potassium oxalate monohydrate ($K_2C_2O_4.H_2O$), *tert*-butanol ($(CH_3)_3OH$), *p*-benzoquinone ($C_6H_4O_2$), and carbon tetrachloride (CCl_4) are used as a hole (h^+), hydroxyl radical (OH·), superoxide radical (O_2^-), and an electron (e^-) trapping agents [9]. The overall photocatalytic procedure for this experiment is similar to that described for the green laser experiment.

2.5. Photoconductivity measurement

The typical operational procedure for photoconductivity measurement is as follows. Initially, Au electrodes are fabricated on a precleaned glass substrate via sputtering, leaving a channel width of 50 μm (Fig. S1). A homogeneous slurry of the catalyst is drop-casted on the channel. The current-voltage (I-V) measurements are performed in a sweep mode under ± 5 V at a scan rate of 0.01 $Vsec^{-1}$, using the KEITHLEY 2634 B source meter.

2.6. Density functional theory (DFT) calculations

All theoretical calculations have been performed using the DFT formalism built-in Gaussian 09 program package. The ground-state geometry of the CN nanosheet has been optimized employing the B3LYP functional and 6−311 G (d,p) basis set. LanL2DZ basis set is chosen for the Au and Ag atom to optimize the CN nanosheet-Ag/Au complex.

2.7. Optical simulations

We performed an optical field simulation study with finite element method (FEM) based COMSOL Multiphysics 5.2 (wave optic module) software to frame the possible optical interaction scenario in the bimetallic system. This simulation study provides information about the distribution of optical fields due to the interaction of an incident EM field with the Ag and Au NPs by numerically solving Maxwell's equations for the system.

3. Results and discussion

3.1. Structural, morphological, and compositional study

The size and morphology of the bimetallic composites with different Ag/Au precursor ratios are shown in the HRTEM images (Fig. 1). In all the composites (Fig. 1a–e), we see well distributed Au and Ag NPs over the CN nanosheet. We have determined size distributions of Ag and Au NPs for each compositions (Fig. S2). The average size of Ag for each composition is as follows: 6.93 nm (C19), 8.44 nm (C37), 8.05 nm (C55), 11.57 nm (C73), 12.44 nm (C91). Similarly, for Au NPs, the average sizes are as follows: 41.7 nm (C19), 34.2 nm (C37), 13.8 nm (C55), 41.5 nm (C73), and 34.5 nm (C91). Thus, we see that the Ag NPs have comparatively smaller sizes than Au NPs. Fig. 1f–h shows the high-resolution images of C55 (f-g) and C91 (h). Literature reports reveal that $AgNO_3$ concentrations are crucial in Au nanostructures' growth and shape evolution [32]. Thus, we infer that Ag precursors play a similar role in the growth of Au NPs during the synthesis process.

While determining the size distributions, we have chosen the high contrast particles as Au NPs and the light dots as Ag NPs. However, from the images, it is not easy to find a clear distinction between Ag and Au

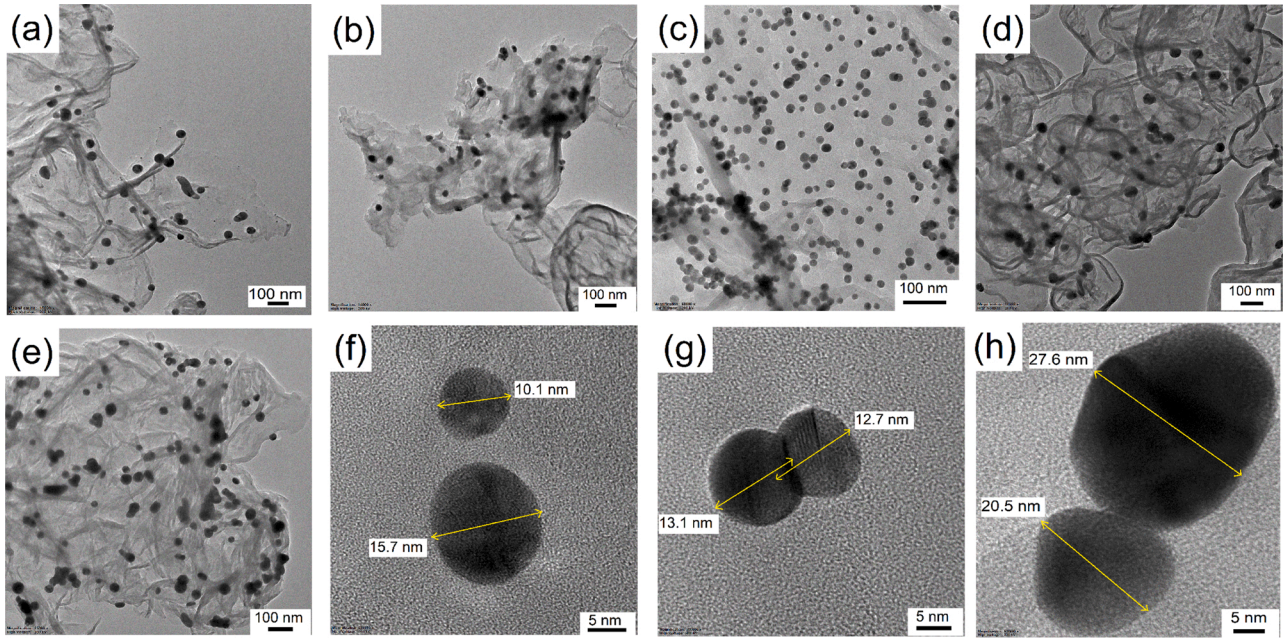

Fig. 1. HRTEM images of (a) C19, (b) C37, (c) C55, (d) C73 and (e) C91. The high-resolution images of C55 (f, g) show spherical shapes of Ag and Au. Slight deformation in their shapes is seen in C91 (h).

NPs. Therefore, we took TEM color mapping to identify the elements in the bimetallic composite (C55). Fig. 2a shows the TEM image of C55, and Fig. 2b–e shows the color mapping of individual elements. The mapping shows that the red dots of Au NPs (Fig. 2b) match the high contrast spherical particles in Fig. 2a, and the scattered green regions in Fig. 2c matches the low-contrast spherical particles in Fig. 2a. The dense particles of C and N are shown in Fig. 2d, e. Fig. 2f shows the XRD pattern of the bimetallic systems with various Ag/Au precursor ratios. The two distinct peaks at 27.7 ° and 12.8 ° in pristine CN are indexed to (002) and (100) crystallographic planes. The diffraction peaks of Au and Ag conform to their cubic structures and are appropriately tagged in Fig. 2f. The peaks at 32.2 ° and 46.2 ° in C37, C55, and C73 emerge due to the fractional distribution of AgO and Ag_2O over CN nanosheets [15, 25,33].

The chemical composition of the prepared composite is analyzed with XPS. Fig. 3 shows the core-level C 1s and N 1s spectra of CN, C55, and C73. The broad C 1s spectrum of C55 is deconvoluted into four peaks at 284.91 eV, 286.27 eV, 288.07 eV, and 288.97 eV. The prime peak at 288.07 eV is attributed to C—N═C bonding. Other peaks are due to reference C—C bonding (284.9 eV), C—O—C bonding (286.27 eV), and O—C═O bonding (288.9 eV) [15,25]. The fitted results are incorporated in Table S1. The satellite peak due to π-π* excitation appears towards high binding energy (B.E.) in some bimetallic composites. The N 1s spectrum of C55 is fitted into three peaks, as shown in Fig. 3d–f. The peak at 398.62 eV is due to two coordinated N-atom (N_{2C}) in the —C═N—C aromatic ring and the peak at 399.65 eV is due to three-coordinated (N_{3C}) tertiary N—$(C)_3$ group in the aromatic ring or at the bridging sites. The third peak at 400.89 eV arises due to C—NH bonding. The small peak around 404.16 eV is because of charged nitrogen [15,34]. The deconvoluted C1s and N1s spectra of the remaining samples are shown in Fig. S3. The fitted peak positions in CN and the remaining bimetallic samples are shown in Table S1.

Au 4*f* spectra of bimetallic samples C55, C73, C91 are shown in Fig. 4a–c. The deconvoluted spectrum of C55 shows major doublets at 83.92 eV ($4f_{7/2}$) and 87.64 eV ($4f_{5/2}$) with a separation of 3.72 eV, confirming the metallic state of Au^0. Two shoulder peaks also appear near the major doublets. The energy difference between the parent and the shoulder peak corresponds to the oxidized forms of Au^+ (Au_2O) [15, 35]. The fitted peaks of other samples also show the presence of Au^+. The fitted parameters are shown in Table S1. The deconvoluted core-level Ag 3d XPS (Fig. 4d–f) of C55 shows major doublets at 368.24 eV ($3d_{5/2}$) and 374.28 eV ($3d_{3/2}$). The difference of 6 eV between the two peaks confirms the metallic state of Ag^0. Two shoulder peaks emerge at a higher B.E. side of the major doublets in C55. These shoulder peaks are because of Ag^+ [36]. The Au 4f and Ag 3d spectra of C19 and C37 are shown in Fig. S4. XPS, thus, reveals that the bimetallic composition contains a metallic state and oxidized forms of both Au and Ag.

The band edge positions of CN are determined with UPS and valence band XPS (VB-XPS) (Fig. 5). The intersection point of the fitted linear edge of the curve with the flat energy distribution in VB-XPS spectra gives the value of valence band energy (E_v) to the Fermi level (E_{FE}) of the semiconductor [37,38]. From the UPS spectra, the work function of Ag/Au bimetal decorated CN is calculated as [39]-

$$\Phi = h\nu - (E_{FE} - E_{SE})$$

Where $h\nu$ is the excitation energy and the value is 21.22 eV for He I source.

(E_{EE}-E_{SE}) gives the width of the UPS spectra. E_{FE} is the Fermi edge and is determined as the intersection point of the extrapolated linear portion of the ordinate with the higher KE abscissa. E_{SE} is the secondary cut-off edge and is determined as the intersection point of the extrapolated linear portion of the ordinate with the abscissa towards the lower KE end.

In our analysis, as shown in Fig. 5b, the value of E_{FE} and E_{SE} are found to be 21.08 eV and 4.90 eV, respectively. Therefore, the work function (Φ) is calculated to be 5.04 eV. It gives the Fermi level position at E_F = 5.04 eV on the vacuum scale. The valence band maximum (VBM) and conduction band minimum (CBM) is obtained by considering the relations- VBM= Φ + E_v and CBM = BG-VBM respectively, where BG is the

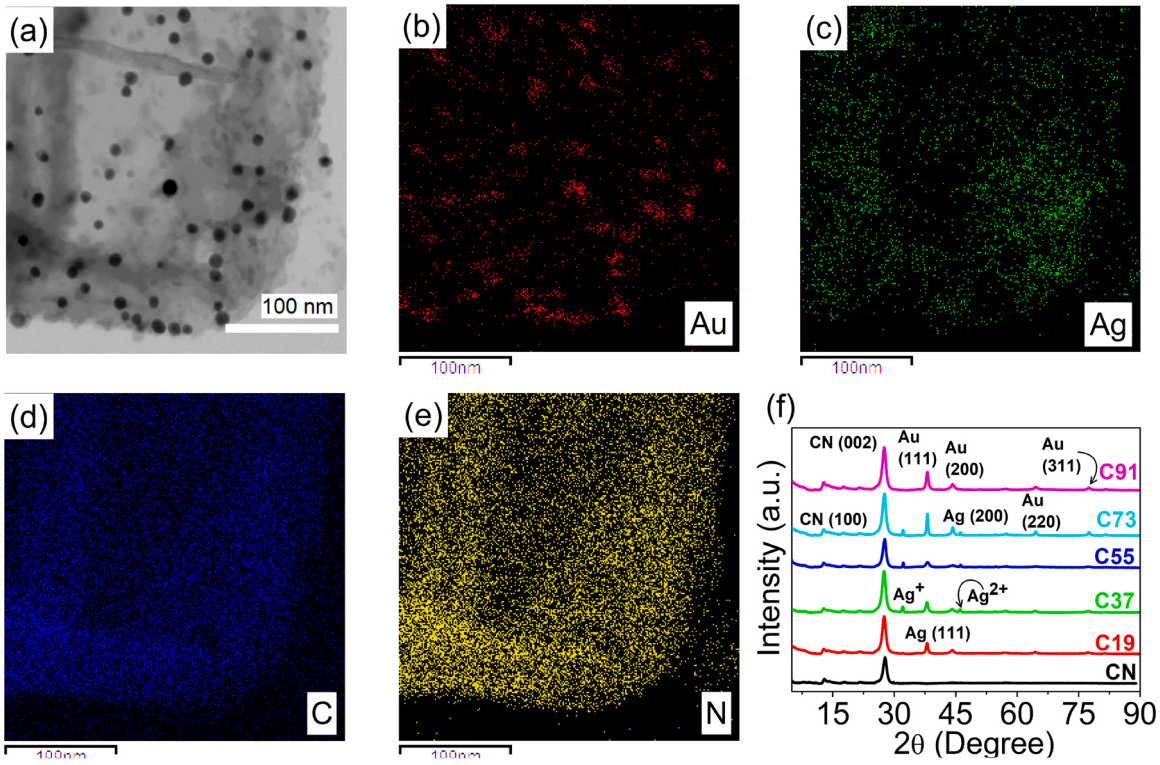

Fig. 2. (a) TEM image of C55. Colour mappings of (b) Au, (c) Ag, (d) C, and (e) N. (f) XRD pattern shows the diffraction lines corresponding to Ag, Au, and their oxidized forms (Ag^+ and Au^+) for various compositions.

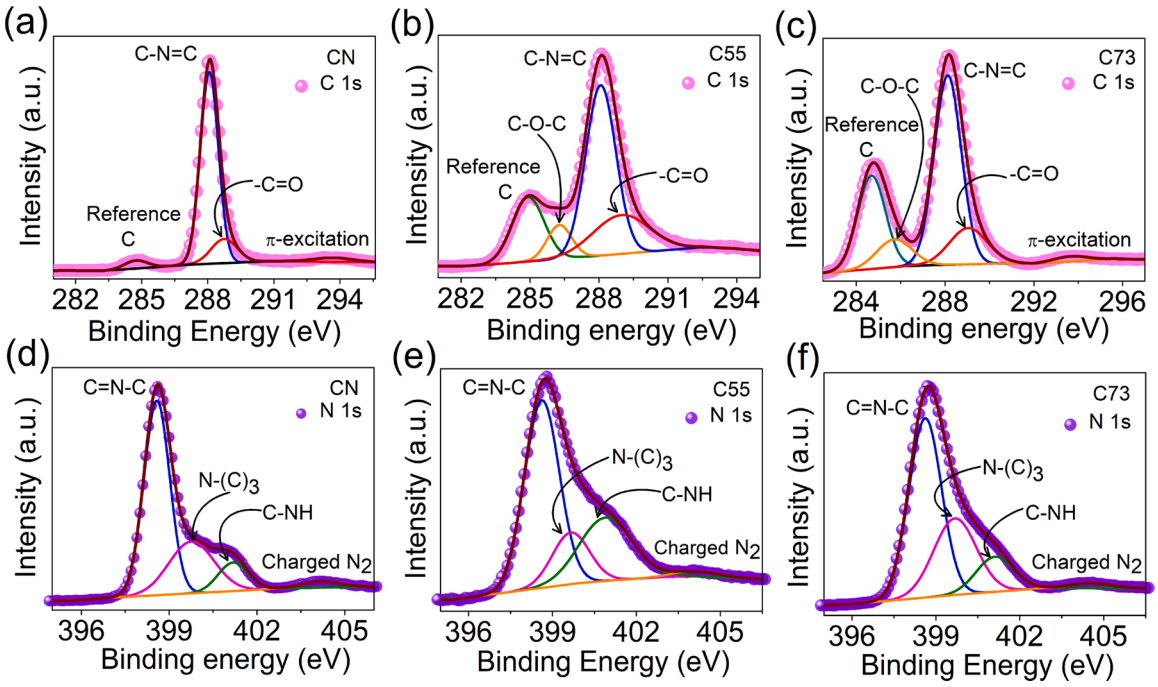

Fig. 3. Core level C 1s (a–c) and N 1s (d–f) spectra of CN, C55, and C73.

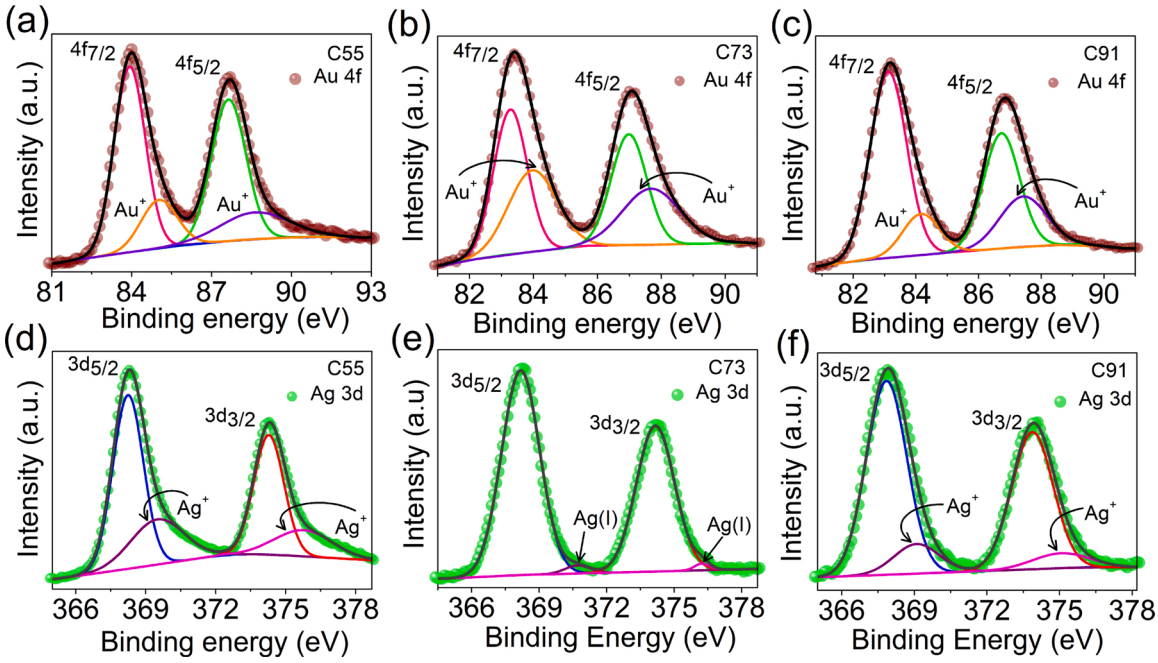

Fig. 4. Core level Au 4f (a–c) and Ag 3d (d–f) spectra of C55, C73, and C91.

band gap of CN. E_v is calculated to be 0.36 eV as shown in inset of Fig. 5a.

3.2. Electronic property calculation

The alteration of the localized structure of CN on bimetal deposition is further studied using DFT. The DFT calculation shows the interaction between the bimetals and the CN nanosheets containing nitrogen-vacancy defects. The optimized structure is provided in scheme-I and scheme-II of Fig. 6a, b, respectively. Scheme-I shows the deposition of Ag/Au bimetals on the N vacancy site via the Au atom. In Scheme-II, we have deposited Ag/Au bimetals on the N vacancy site via the Ag atom. The bimetals get connected with the carbon atom and lead to a slight distortion of the ring. The structural modification is similar in both schemes. We have calculated the band gap ($\Delta_{H\text{-}L}$) values of the optimized samples, and the results are shown in Table 1. $\Delta_{H\text{-}L}$ is the difference in the energies between the highest occupied molecular orbital (HOMO) and lowest unoccupied molecular orbital (LUMO) [40,41]. From Table 1, it is observed that the $\Delta_{H\text{-}L}$ values of the Ag/Au bimetal-CN nanosheet complexes decrease compared to the CN nanosheet.

The density of states (DOS) can be defined as the number of different

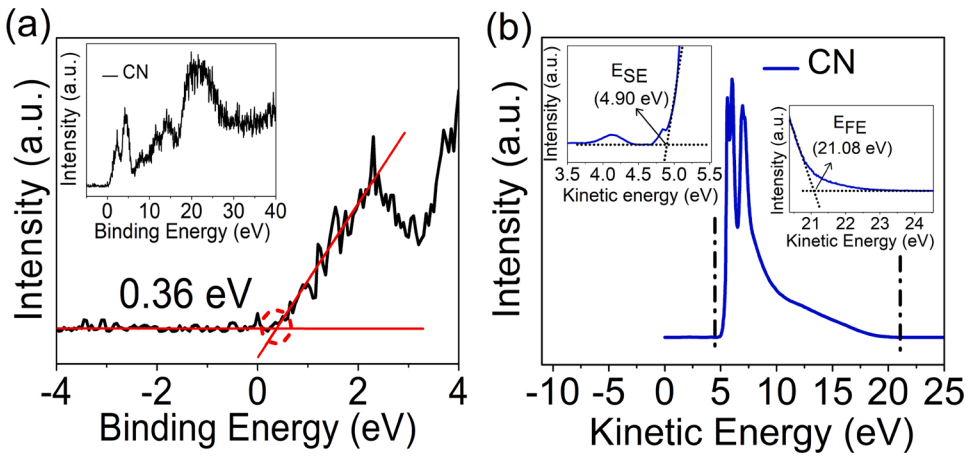

Fig. 5. a) Valence band (VB) energy calculated from VB-XPS spectra (inset of (a)). (b) UPS spectra of CN. The inset of (b) shows the Fermi edge (E_{FE}) and secondary cut-off edge (E_{SE}).

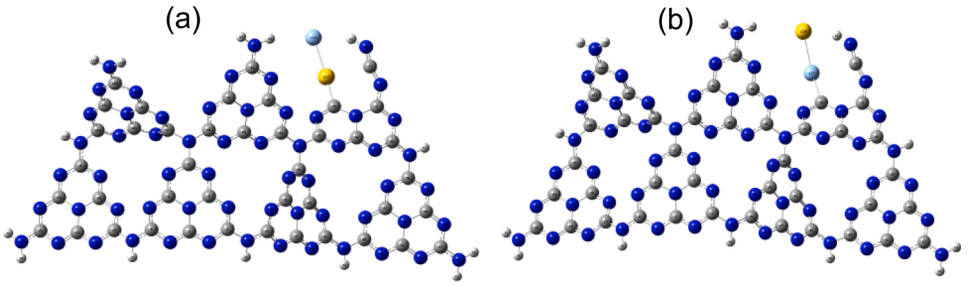

Fig. 6. Optimized structures of the complexes (a) Scheme-I (b) Scheme-II. The yellow sphere represents the Au atom, and the blue sphere represents the Ag atom. Grey and blue spheres represent C and N in g-C_3N_4 (For interpretation of the references to colour in this figure legend, the reader is referred to the web version of this article).

Table 1
Energies of HOMO, LUMO and $\Delta_{H\text{-}L}$ values of the studied complexes.

Complex	E_{HOMO} (eV)	E_{LUMO} (eV)	$\Delta_{H\text{-}L}$ values (eV)
CN nanosheet	−6.31	−2.66	3.65
Scheme-I	−4.90	−2.53	2.37
Scheme-II	−5.73	−2.57	3.16

states at a particular energy level an electron can occupy. The partial density of states (PDOS) is the relative contribution of a particular atom or orbital to the total DOS [42]. A correlation of the frontier molecular orbitals (FMOs) with the electronic structures can be established to calculate the partial density of states (PDOS) of the compounds. PDOS is calculated using the GaussSum software. The computed PDOS spectra (Scheme-I) show that the bimetals contribute 83 % to the HOMO (or VB) and 2 % to the LUMO (or CB). CN nanosheet has 17 % and 98 % contribution to the HOMO and LUMO, respectively. PDOS spectra for Scheme-II reveals that the bimetals have contributed 80 % to the HOMO and 5 % to the LUMO, whereas CN nanosheet has 20 % and 95 % contribution to the HOMO, LUMO respectively. The plot of PDOS spectra of the complexes is provided in Fig. 7. DFT clarifies that the deposited Ag/Au bimetals contribute more towards the VB of CN. However, the CN nanosheet has a high contribution to the CB. The contribution is coming from the nitrogen vacancies that act as donor

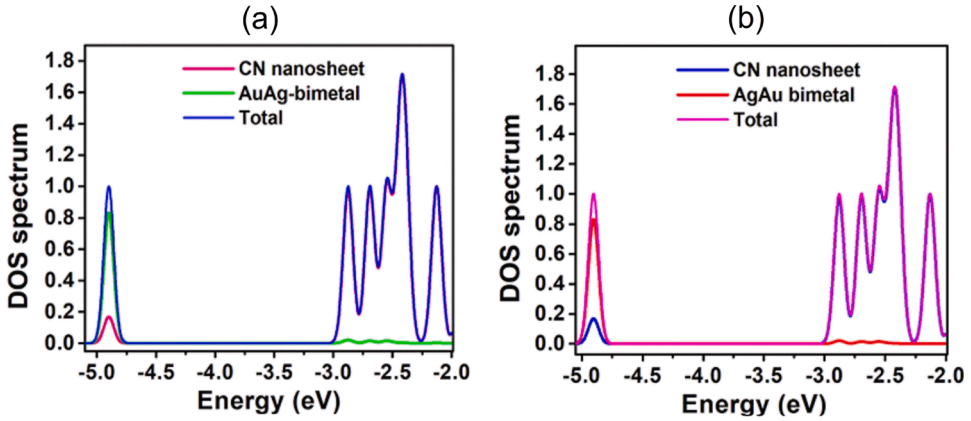

Fig. 7. The plot of PDOS spectra of the complexes. (a) Scheme-I (b) Scheme-II.

states and contribute towards the CB.

3.3. Optical properties study

Fig. 8 shows the UV–vis DRS of the bimetallic composites. The pristine and composite systems show an excitonic absorption at 370 nm. The localized surface plasmon resonance (LSPR) of Ag at 480 nm is seen in C19 containing a high Ag. However, as the amount of Au increases, the LSPR of Ag is damped or quenched. The LSPR of Au at 532 nm remains unchanged in various Ag/Au compositions.

Steady-state and TRPL spectroscopy measures the photoinduced carrier dynamics in the bimetallic system. Fig. 9a shows the steady-state PL spectrum of CN at a photoexcitation of 375 nm. The spectrum shows a single excitonic emission at 460 nm. This peak quenches in intensity after loading the bimetals. Quenched emission intensity indicates dissociation of excitons into free electrons and holes and their subsequent separation. The recombination inhibition is arguably due to the charge transfer from CN to the bimetals. The lifetime of photoinduced carriers is determined with TRPL. Fig. 9b shows the TRPL results of CN and C55 at an excitation of 375 nm. For convenience we have reported the TRPL of C55 here. A tri-exponential fitting can best suit the temporal decay in emission intensity. Table 2 shows the extracted carrier lifetime and the amplitudes from the fitting. For CN, τ_1 originates from exciton localized on the s-heptazine ring, and τ_2 originates from exciton migration and subsequent recombination at a site along a stacked (interplanar) direction. The long-component τ_3 originates from exciton migration along the interplanar chain and their subsequent recombination at defect or dopant site [34,43]. After bimetal decoration, τ_1 shortens while τ_2 and τ_3 increase. The short component is mediated by any oxidized forms of Au^+ and Ag^+, dissociating the exciton and facilitating the carrier recombination. The long component indicates charge transfer from CN and trapping by the bimetals. By using the relation $(\tau_{Semi}\tau_{Hybrid})/(\tau_{Semi}\text{-}\tau_{Hybrid})$, we have measured the charge transfer (τ_{CT}) time and charge transfer efficiency (η) [44,45]. As Table 2 shows, the charge transfer time is 9.07 ns with only 21 % efficiency. The poor charge-transfer efficiency is possibly due to the trapping of photogenerated electrons by the interfacial Ag^+ and Au^+ [15].

3.4. Photoconductivity measurement

Photoconductivity measurement is conducted to test the generation of hot photocarriers from the metallic systems through interband *d-sp* or intraband (SPR) excitation under selective photoexcitation [45–47]. The interband transition releases hot electrons near the Fermi surface in the *sp*-band and holes in the *d*-band. SPR decay produces hot electrons with energies extending above the Fermi surface [30,45]. The interband transition of Ag occurs in the UV region (>380 nm), and that of Au spans from its near SPR absorption to the UV region (320−540 nm) [30]. We have performed the I-V measurement at 420 nm and 525 nm under a sweeping voltage of ± 5 V (Fig. 10). Photocurrent measures the differences in the current obtained under illumination and in the dark. We have shown the dark current for all the samples in Fig. S5. The maximum recorded photocurrent of 7.8 nA for C73 at 420 nm is 2-times higher than C55 and 20 times higher than pristine CN (Fig. 10a). By considering the absorption positions of Ag and Au NPs in the colloidal solution and the composite, we infer that the large photocurrent in C73 and C55 is contributed by hot carriers generated through SPR excitation in Ag NPs and interband transition in Au NPs [30,45–47]. Of note, we could not derive a benefit in photocurrent response with 525 nm excitation for the bimetallic samples, although it matches the SPR of Au NPs (Fig. 10b). At 525 nm, pristine CN delivers the maximum photocurrent of 0.26 nA followed by 0.23 nA in C73 (Fig. 10b). If we notice, the same bimetallic sample (C73) shows a much higher photocurrent under 420 nm than at 525 nm. Despite a band gap of 2.7 eV (459.2 eV), the comparatively large photocurrent in CN is caused by carriers trapped in the intermediate defect states. We have provided the following probable causes for the reduced photocurrent in the composites under 525 nm excitation. First, a fraction of the plasmon-induced carriers undergo radiative decay because of the close Fermi surfaces of Ag and Au, providing less available free carriers for photocurrent. Second, the oxidized Ag^+ and Au^+ surface states might capture the SPR activated hot electrons and contribute to a reduced photocurrent. The negative photocurrent in C19 is possibly due to the decreased mobility of photocarriers [48].

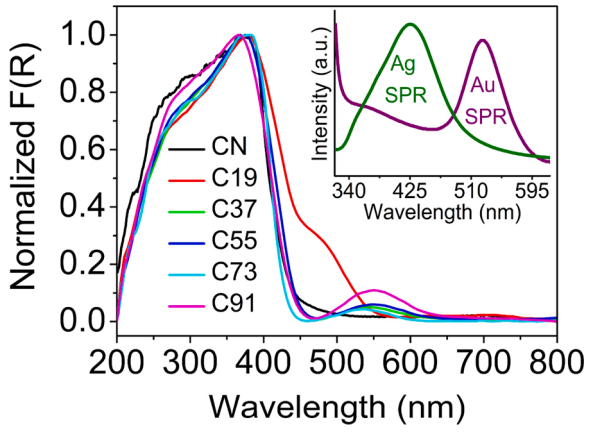

Fig. 8. Kubelka-Munk absorption spectra of CN and bimetallic samples.

3.5. Optical simulation study

The optical simulation is conducted to measure the EM field intensity at the nearest gap between Ag/Au nanoparticles. A strong near-field could expedite hot-electron generation and PIRET. For conducting the optical simulation, we have chosen the sizes from the TEM image of C55 (Fig. 2a). Since we have taken color mapping of C55, the identification of Ag and Au NPs become easy for finding the particle sizes and interparticle separation. We are repeating Fig. 2a as Fig. 11a only for devising the framework for optical simulation. The particles size distributions of Ag and Au NPs from Fig. 11a is shown in Fig. S6. The average size for Au and Ag NPs are 12 nm and 7 nm, respectively. From the TEM micrograph in Fig. 11a, we have derived situations in which two equal and two unequal sizes of Ag and Au NPs are at a fixed separation of 2 nm. Plane polarized lights of wavelength 500 nm and 410 nm are allowed to incident normally on the plane containing the Ag and Au NPs. An increase in separation distance from 2 to 5 nm and 10 nm reduces field intensity, as seen in Au dimmers case (Fig. S7a–c).

If we consider a situation in which two Ag NPs (7 nm) are separated by 2 nm, the simulated field intensity is 9×10^6 at 410 nm excitation (Fig. S7d). If we replace one Ag NP with Au NP, the field intensity at 410 nm reduces to 5.25×10^6, and the field is more localized on Ag NPs (Fig. 11b). For a similar configuration, at 500 nm excitation, the field intensity of magnitude 3×10^6 is concentrated at the inter-gap of Ag-Au (Fig. 11e). In Fig. 11c, 7 nm Ag NP attached to 13 nm Au NP produces a field intensity of 7×10^6 with the field concentrated on Ag NP (Fig. 11c). However, if the situation is reversed and a 7 nm Au is attached to 13 nm Ag, the simulation generates a field intensity of 6×10^6 with intensity localized at the interparticle gap (Fig. 11d). For a similar scheme (Fig. 11f, g), the excitation at 500 nm generates much-reduced field intensity than 410 nm excitation. Further, the magnitude of the field intensity remains the same and is localized at the gap region in all the interparticle configurations (Fig. 11e–g). Hence, excitation of 410 nm produces a much stronger field intensity than 500 nm excitation in the bimetals. Likely, the *d-sp* interband transition in Au NPs and SPR excitation in Ag NPs contributes to intense field intensity at 410 nm. The reduced electromagnetic field intensity at 500 nm is possibly caused by the damping of plasmonic excitation of Au by its corresponding interband transition at 500 nm.

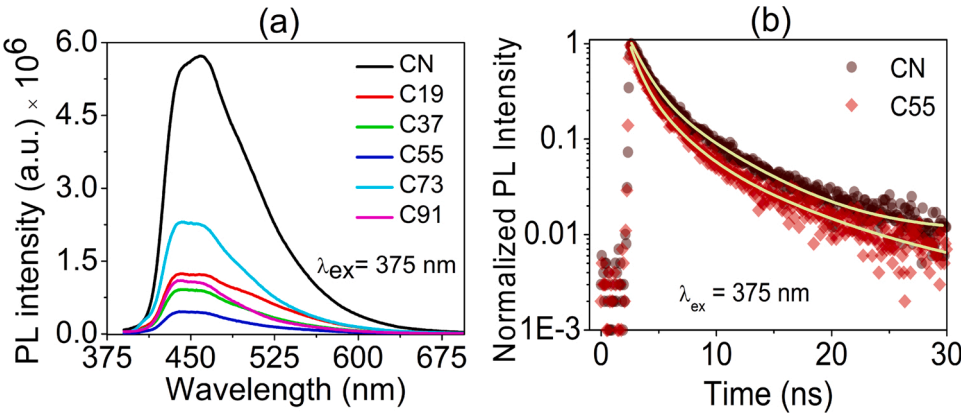

Fig. 9. (a) Steady-state PL spectra of the samples at an excitation of 375 nm. (b) TRPL spectra of CN and bimetallic sample C55 at an excitation of 375 nm.

Table 2
Fitted components of lifetime, amplitude, charge-transfer efficiency for the pristine and bimetallic composite.

SAMPLE	$\tau_1(A_1)$ ns	τ_2 (A_2) ns	τ_3 (A_3) ns	τ_{av} ns	τ_{CT} ns	η(efficiency) %
CN	1.36 (0.47)	1.37 (0.44)	5.29 (0.09)	2.5	–	
C55	0.79 (0.91)	2.45 (0.08)	8.36 (0.01)	1.96	9.07	21

3.6. Photocatalytic study

We have selected three radiation sources for studying photocatalysis: UV, UV–vis, and green laser (532 nm). The activity of the photocatalysts under light is measured by subtracting the absorption of RhB under 45 min of dark stirring. Upon UV light shining, C91 offers a maximum of 53.28 % degradation of RhB, whereas it is only 10.8 % with pristine CN (Fig. 12a). All the bimetallic systems show a better activity in RhB degradation than CN. The photodegradation rate of RhB is evaluated with a pseudo-first-order rate kinetics, $\ln(C_t/C_0) = -kt$, where k, C_0, and C_t are apparent rate-constant, initial concentration, and concentration after a time t. The measured rate constant for C91 (0.0091 min^{-1}) is 9 times higher than that of CN (0.0011 min^{-1}) (Fig. 12d). Next, we checked the photocatalytic activity of the samples under UV–vis light (Fig. 12b). Surprisingly, we could not see any satisfactory results in the bimetallic composites compared to the pristine CN. CN91 displays a nearly comparable photocatalytic activity to CN, while for other compositions, the activity is lower than CN. The maximum degradation of RhB achieved with CN is 91 %, whereas it is 89.5 % with C91 at 105 min of irradiation. A linear pseudo-first-order fitting is performed between 0–45 min and 45–90 min. We have got k_1~0.0183 min^{-1} and k_2~0.046 min^{-1} for CN. The rate constants for RhB degradation with C91 is 0.0259 min^{-1} (k_1) and 0.073 min^{-1} (k_2) (Fig. 12e).

The last experiment on photocatalysis is tested with green laser excitation. We observe a 50 % removal of RhB (Fig. 12c) by CN with an apparent rate constant of 0.009 min^{-1} (Fig. 12f). Amongst the bimetallic catalysts, C73 shows a maximum of 42.1 % RhB degradation (Fig. 12c) with a rate constant of 0.007 min^{-1} (Fig. 12f). Our earlier study has shown that Ag-CN and Au-CN deliver better RhB removal performance under monochromatic green light excitation than pristine CN [15]. The present study shows that bimetal deposition has a retarding effect on the overall photocatalysis under UV–vis and green laser. Therefore, we argue that a "plasmonic quenching" rather than a "plasmonic activation" process impacts photocatalysis under UV–vis and green laser.

A repeated photocatalytic experiment checks the heterogeneity and stability of the prepared photocatalysts. The procedure is already mentioned in the experimental section. RhB degradation with C73 after 1st, 2nd, and 3rd cycle are 42 %, 40.9 %, and 36.6 %, respectively. In this test, until the end of the third cycle, the C73 catalyst is recycled for 5.25 h. After the 3rd cycle, we measure a 5 % loss in photocatalytic activity. The minimal loss signifies that sample heterogeneity is retained. However, to measure possible metal ion leaching during the experiment, we took EDX of the pristine and recovered catalysts (1st and 3rd cycle) (Fig. S8). The composition is checked at two different locations, and the differences of Ag and Au content on the surface are quite visible. The quantified values of Ag and Au are shown in the insets of Fig. S8. C73, after the 1st and 3rd cycle, has a slightly low content of Ag and Au. Therefore, we might consider that a percentage of Ag and Au are leached into the solution during recycling. Further, we took XRD to test

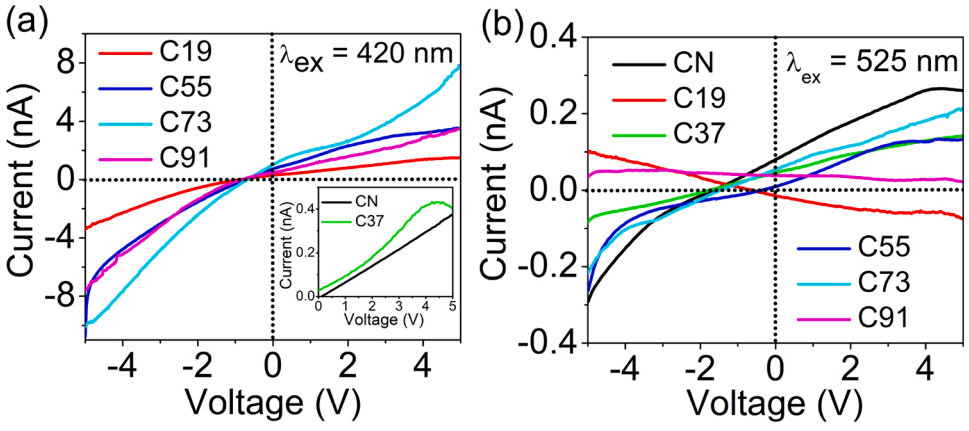

Fig. 10. I-V characteristic curves of the catalysts under (a) 420 nm, (b) 525 nm LED excitation.

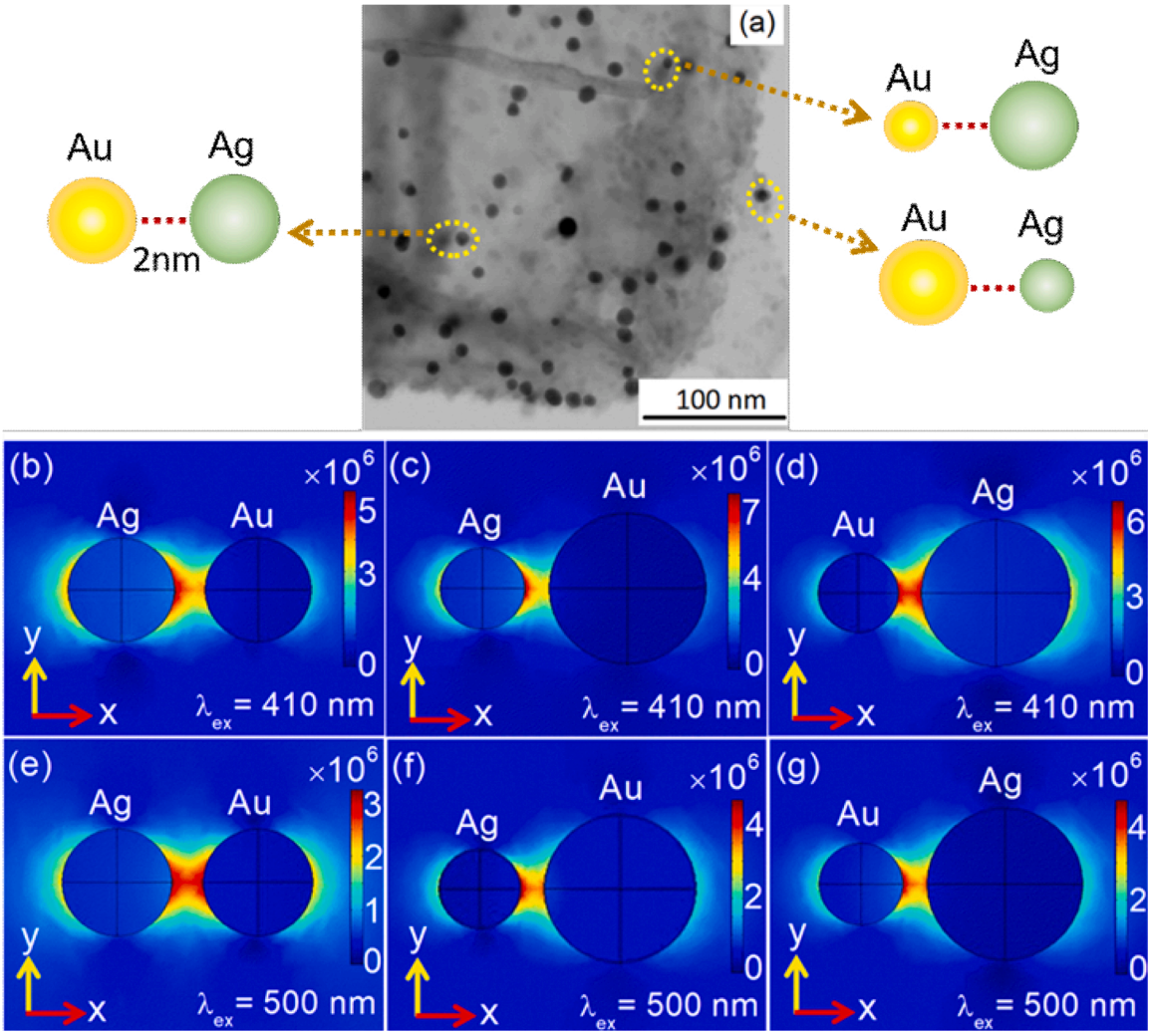

Fig. 11. (a) The size of the Au and Ag for simulation is taken from the TEM image. (b)–(d) COMSOL simulation of optical field intensity for Au and Ag NP at excitation of 410 nm. (e)–(g) COMSOL simulation of optical field intensity for Au and Ag NP at excitation of 500 nm.

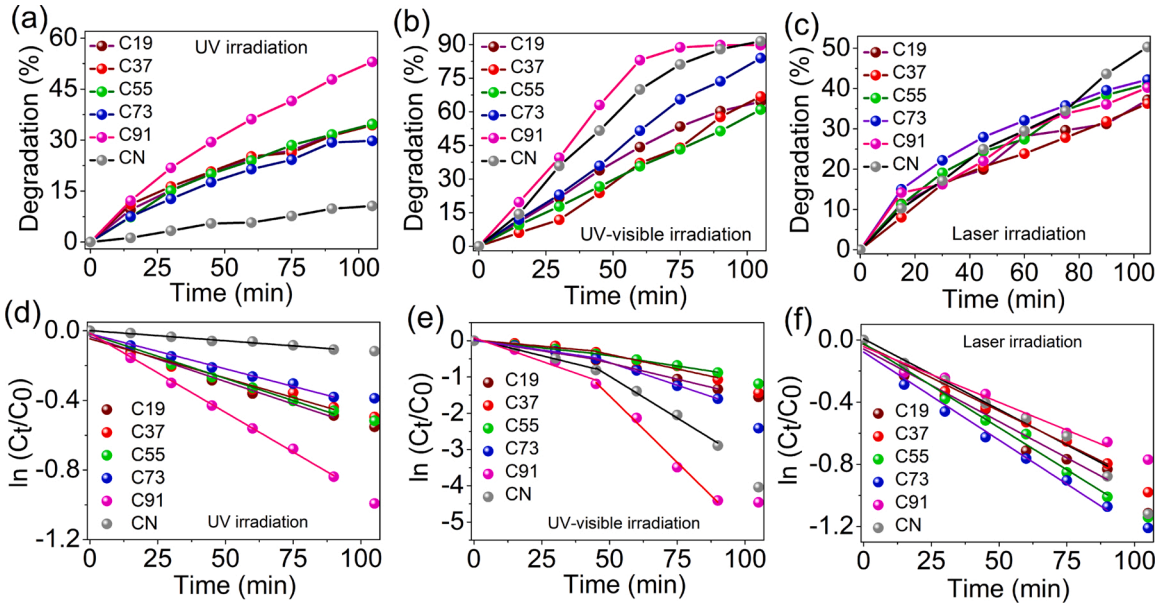

Fig. 12. Degradation curves (a–c) and first-order rate kinetics (d–f) of pristine and bimetallic composites under UV, UV–vis, laser radiation.

crystallinity in the leached/recycled samples (Fig. 13b). There is no loss in crystallinity, and the intensity of Au remains the same after the test. The disappearing AgO or Ag_2O peak intensity is possibly due to the photoreduction of Ag_2O to Ag metals or due to Ag ion leaching. A similar cyclic test with CN shows RhB degradation of 50.3 %, 49.5 %, and 42 % for the 1st, 2nd and 3rd cycle, respectively (Fig. S9a). We also took XRD of CN (Fig. S9b).

The reactive species that aid the photodegradation are electrons (e^-), holes (h^+), hydroxyl (OH), and superoxide radicals ($O_2^{\bullet-}$). To identify the active radicals promoting photocatalysis in C73, we have performed radical scavenging tests. It is found that the degradation is not much affected by the trapping of hydroxyl radical ($OH^\bullet$) and electrons (e^-) (Fig. 13c). In the presence of di-potassium oxalate monohydrate ($K_2C_2O_4.H_2O$), which acts as a hole (h^+) scavenger, the degradation is reduced to 31.33 %. However, the presence of superoxide ($O_2^{\bullet-}$) scavenger that is *p*-benzoquinone ($C_6H_4O_2$) reduces the degradation to a negligible value of 3.26 %. It, thus, infers that superoxide radicals play a crucial role in the effective photodegradation of RhB.

3.6.1. Mechanism of photocatalysis

The charge transfer pathways of photogenerated carriers and the photocatalysis mechanism require an idea of the band structure of the composite. We have deduced the band structure based on the results obtained from VB-XPS and UPS spectra. The constructed band structure (Fig. 14a) shows that the Fermi levels of Ag and Au NPs lie very close to the VB of CN. The results of DFT further support this observation. DFT also states that bimetals contribute more to the VB of CN. We have drawn the charge-transfer pathways in the heterostructure under illumination based on these results and observations.

3.6.2. Under UV radiation

The charge transfer/recombination pathways (b1-b5) under UV irradiation are shown in Fig. 14b. Upon UV irradiation (250−380 nm), semiconductor excitonic transition and metals interband transition coincides. Photoexcitation of CN releases carriers with a short lifetime (Table 2). It, thus, records an insufficient photocatalytic activity in pristine CN. In bimetallic composites, the photoinduced electrons are transferred from CN to the bimetals (b1). This charge transfer process acquires a poor efficiency ($\eta = 21.1$ % from TRPL) because of Ag^+ and Au^+ interfacial electron trap states. Thus, limited numbers of carriers remain available over CN and the bimetals. As discussed, UV light promotes interband (*d-sp*) electronic transition and releases hot electrons near the Fermi surface (E_f) of Ag and Au NPs (b2, b3) [30,45–47]. To ensure that hot electrons are generated in Ag/Au, we have performed an I-V measurement at 365 nm. As Fig. S10 shows, the bimetallic samples show a much-enhanced photoresponse compared to pristine CN. The highest photocurrent shown by C91 is 9 times stronger than that of CN. The strong photocurrent in C91 under UV photons is due to hot electrons generated by interband excitation. The bimetallic surface stores the hot electrons as well as the electrons transferred from CN. Because of the nearest Fermi surface of Ag/Au with the VB of CN, a handful of the Fermi electrons may undergo recombination with the holes in the VB of CN (b4, b5). The remaining electrons over the bimetals and CN and holes on the *d*-band of Ag/Au might participate in the generation of reactive oxygen species for photocatalysis.

3.6.3. Under UV–vis excitation

As discussed, we have recorded a reduced UV–vis photocatalytic activity for most of the bimetallic systems. It is in contrast to our speculation that bimetals could enhance photocatalytic activity. In pristine CN, photoexcited interband and defect carriers are sufficient to degrade RhB. However, for the bimetallic composites, carriers are extracted from CN and are populated over the bimetals. The possible pathways of charge transfer are shown schematically in Fig. 14c–e. We have divided the 256−600 nm range into three different illumination ranges: 256−450 nm, 450−500 nm, and 500−600 nm. The reason is to correlate plasmonic phenomena with photocatalysis in each excitation range. Finally, the plasmonic and excitonic phenomena in these ranges are correlated to describe the quenched photocatalysis in the entire 256−600 nm range.

256−450 nm range: In this range, excitonic and interband transitions in Ag and Au occur in unison. The detailed charge transfer

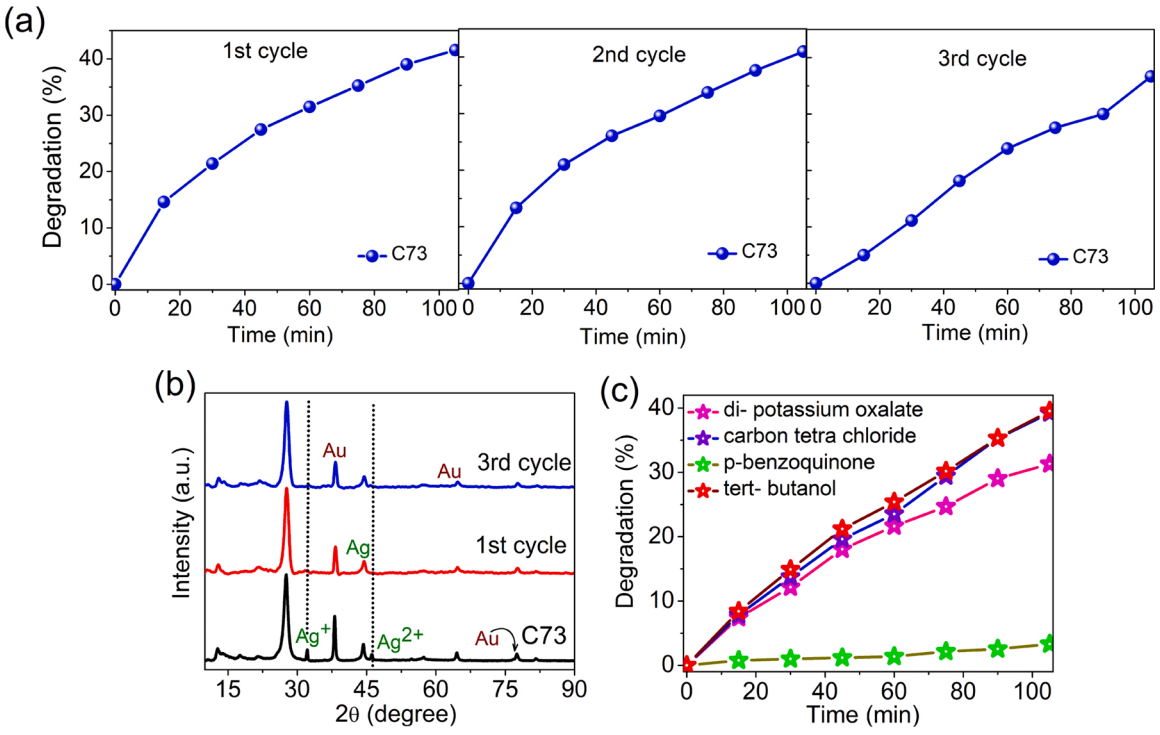

Fig. 13. Photocatalytic activity of (a) C73 tested up to 3 cycles under Laser. (b) XRD pattern of C73 after the 1st and 3rd cycle of reuse. (c) Degradation of RhB in the presence of different scavenging reagents under Laser.

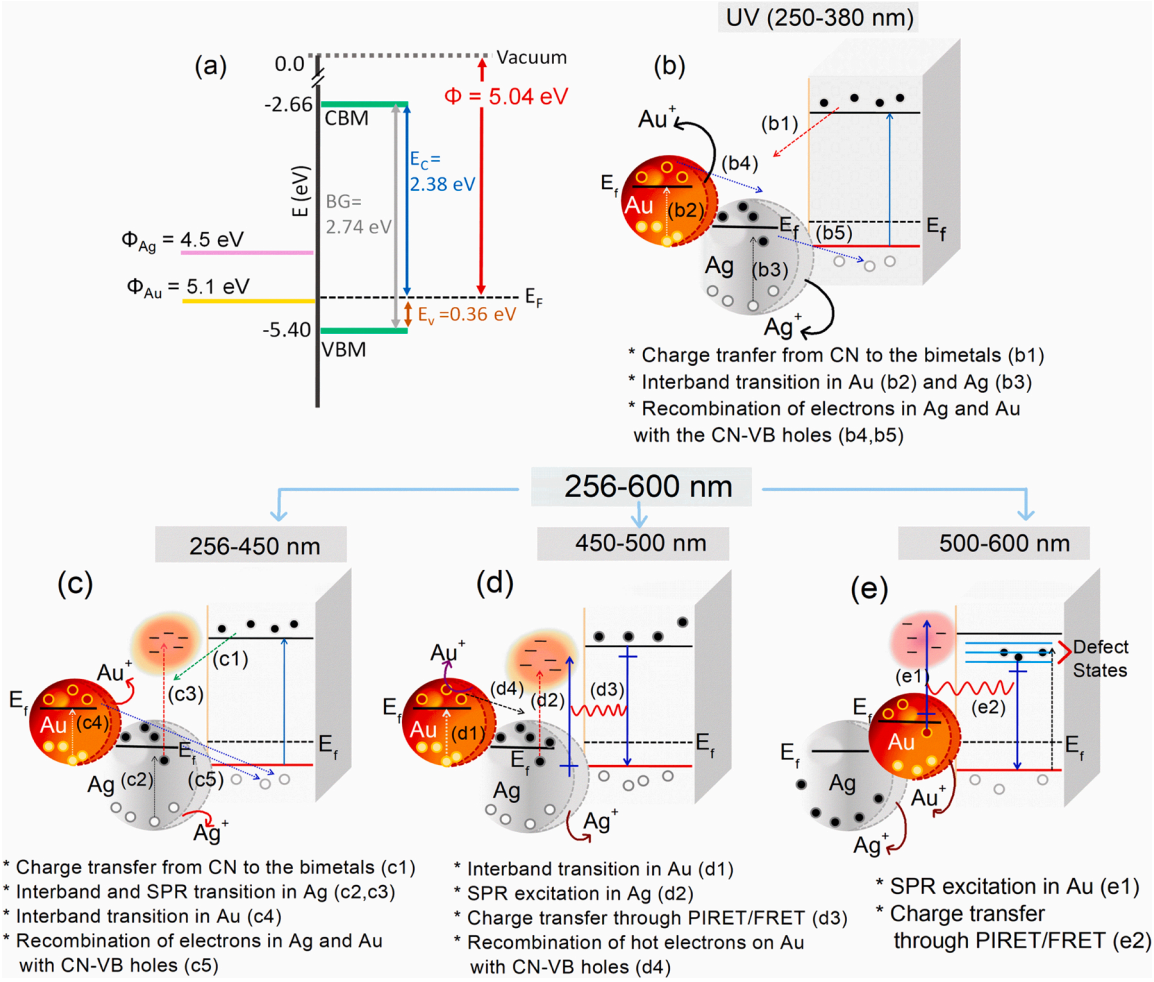

Fig. 14. (a) Band structure of CN analyzed from VB-XPS and UPS spectra along with Fermi level positions of Ag and Au NPs. Schematic mechanism of charge carrier generation and transfer in bimetallic composites under UV (b), UV–vis (c–e) irradiation (256–600 nm). Note: E_F and E_f in the above figures holds similar meaning.

processes (c1-c5) are shown in Fig. 14c. The excited electrons in CN first migrate to the bimetals (c1). The interband transition and SPR decay in Ag promote electrons near the Fermi surface (E_f) and above the Fermi surface, respectively (c2,c3). Similarly, Au also undergoes an interband transition and promotes electrons near the Fermi surface (c4). We have already discussed the probing of hot electrons in the bimetals with I–V measurement and near-field optical simulation. The I-V measurement at 420 nm shows 20 times higher photocurrent in C73 than pristine CN. The high photocurrent is ascribed to hot electrons generation over Ag/Au bimetals through interband transition and SPR decay. Besides, the near-field optical simulation shows the generation of intense electric field intensity at the nearest gap of Ag-Au at 410 nm excitation. The intense optical field at the plasmonic gap also stimulates hot carrier generation over the bimetals and carrier excitation at the near-surface of CN [49]. Once the carriers are accumulated over the bimetals, they undergo recombination through three possible routes: (1) the large near-field will excite hot electrons above the Fermi surface. These hot electrons will migrate to the metal-CN interface for passing on to the CB of CN through the Schottky barrier. The hot electrons might undergo recombination with the interfacial trap centers (Ag^+ and Au^+) and decay. (2) the nearest Fermi surface of Ag and Au NPs might also facilitate recombination of Fermi surface electrons of Au with the available holes in Ag or recombination of the energetic hot electrons in Ag with the sp holes in Au [27,50]. (3) the possible recombination of electrons with the holes in VB of CN, as already mentioned. All these recombination possibilities could reduce the available carriers for photocatalysis. For a simplistic understanding, we have not numbered all of these recombination pathways in Fig. 14.

450−500 nm: Two counteracting energy transfer processes operate in this excitation range besides the interband transition (Au) and SPR excitation (Ag) (d1,d2). These are FRET and PIRET. These processes require spectral overlapping between semiconductor excitation and SPR absorption (d3) [31,51]. FRET takes electrons away from the semiconductor, while PIRET contributes carriers to the semiconductor. Our bimetallic samples show excitonic emission of CN at 450 nm and the SPR absorption of Ag NPs at 450 nm. Since the excitonic emission and SPR absorption occurs at the nearest wavelength, as per theory, there should be spectral overlapping for prevailing both FRET and PIRET. However, the direction of energy flow depends on the metal-semiconductor interfacial distance and the exciton plasmon dipolar strength [31,51]. The oxidized Ag^+ species reduce the SPR dipolar strength, and the close contact with the semiconductor dephases the plasmon energy. Therefore, FRET gets dominance over PIRET. As a result, the photoexcited electrons in CN are carried away to Ag/Au bimetals through FRET. Some of these electrons recombine with the VB holes of CN (d4). The carriers generated through interband, intraband, and FRET occupy bimetallic surfaces. Finally, these carriers undergo recombination through different pathways, as already discussed in the 256−400 nm range.

500−600 nm: In this excitation range, only SPR excitation of Au (532 nm) and sub-bandgap (defect) excitation in CN occurs. SPR excitation releases hot electrons above the Fermi surface (e1). The defect states in CN are distributed just below the CB to the mid band gap [34]. Therefore, as the excitation wavelength approaches the SPR of Au (532 nm) and traps states in CN, both FRET and PIRET are activated (e2).

Similar to the 450−500 nm range, and with a similar argument, we state that the Au^+ states and the close metal-semiconductor interfacial contact is responsible for FRET dominance and driving the carriers away from CN to the bimetals. The I-V measurement at 525 nm shows a reduced photocurrent in the bimetallic system compared to CN (Fig. 10b). The simulation result also shows a reduced electric field intensity at the interparticle gap at 500 nm than at 410 nm (Fig. 11e–g). Ag NPs do not undergo any interband or SPR promotion in this excitation range. However, for Au NPs, SPR excitation and interband transition are equally plausible. Nevertheless, the interband transition and PIRET severely impede the generation of the hot electron in Au NPs. In the absence of any promotional plasmonic effect of Ag, the SPR energy of Au is damped, and thus we see weak optical field intensity and weak photocurrent response, subsequently a poor contribution to overall photocatalysis.

Finally, we have gathered some understanding for the quenched plasmonic photocatalysis under UV–vis light by analyzing the photoinduced phenomena in separate illumination ranges. We have proposed the following reasons for the reduced photocatalytic activity in the 256−600 nm range. First, quenched plasmon energy transfer (PIRET) by FRET. Second, overall plasmon energy damping because of the collective excitation of interband, intraband, and PIRET in this range. Third, recombination of photogenerated carriers over the bimetals, with the oxidized species at the interface, and with the VB holes of CN. All these processes leave the only handful of photocarriers available over CN and bimetals for photocatalysis.

3.6.4. *Under laser (532 nm) excitation*

The carrier promotion and transfer under green laser excitation are similar to the 500−600 nm excitation. The only difference is that the monochromatic excitation activates only those sub-band carriers with which it resonates. For similar reasons cited under UV–vis, FRET is likely to dominate PIRET at 532 nm, leading to reduced photocatalysis. Because of the localized monochromatic excitation, the energy of the generated hot electrons is sufficiently higher than those generated under broadband excitation. Interfacial capturing of the hot electrons by Ag^+ and Au^+ reduces the possibility of movement to CN via the Schottky barrier. The accumulated photocarriers over the bimetals choose several recombination pathways, resulting in a reduced photocatalysis. In pristine CN, the activated carriers from the defects migrate to the interface and generate superoxide and hydroxyl radicals for initiating photocatalysis.

Therefore, the summarized results show that bimetallic sample C91 shows better photocatalytic activity than CN under UV light. Similarly, under UV–vis light, C91 shows a comparable activity with CN in RhB degradation. Under green laser, C91 shows a similar degradation to that of C73. Hence, C91 can be considered as the optimized composition amongst the bimetallic samples with improved photocatalysis. We further pursued our experiment to test the efficacy of the pristine and bimetallic systems for other water contaminants such as methyl orange (MO), methylene blue (MB), and phenol under UV, UV–vis and green laser. The bimetallic composites of C91 and C73 are chosen as they show a better photocatalytic activity in RhB degradation than other compositions. Fig. 15a–c shows the degradation of MO, MB and phenol under UV–vis light. Fig. 15d–f shows the pseudo first-order rate kinetics in the photodegradation of organic pollutants. The degradation plot under UV and green laser irradiations is shown in Fig. S11. The degradations are obtained by subtracting the dark adsorption. The results of degradation obtained under different illuminations are shown in Table S2. Under UV light, the degradation of MO by C73 (26.7 %) and C91 (18.4 %) is higher than that of CN (16.1 %). Similarly, C73 and C91 show better result in phenol degradation than CN under UV. In MB degradation, CN shows better photocatalytic activity (16.4 %) than that of C73 (10.0 %), and C91 (11.4 %). Under UV–vis, the bimetallic systems show better photocatalytic activity in MO and phenol degradation (Fig. 15a, c, Table S2) than CN. A similar result is seen under a green laser (Fig. S1, Table S2). A comparison shows that CN and the bimetallic composites show much better catalytic activity in RhB degradation than MO, MB, and phenol. Phenol records the poorest degradation result. Finally, we can emphasize the various parameters that affect the photocatalytic efficacy of the bimetallic composites. These parameters are interfacial contact and trap centers, Ag/Au compositions in the bimetallic composites, different plasmon-induced phenomena, incident radiation, and nature (cationic, anionic) of the organic contaminant. As the Ag/Au ratio in the bimetallic composite changes, the size distribution for each composite also changes, affecting the interband transition, SPR spectral properties, and

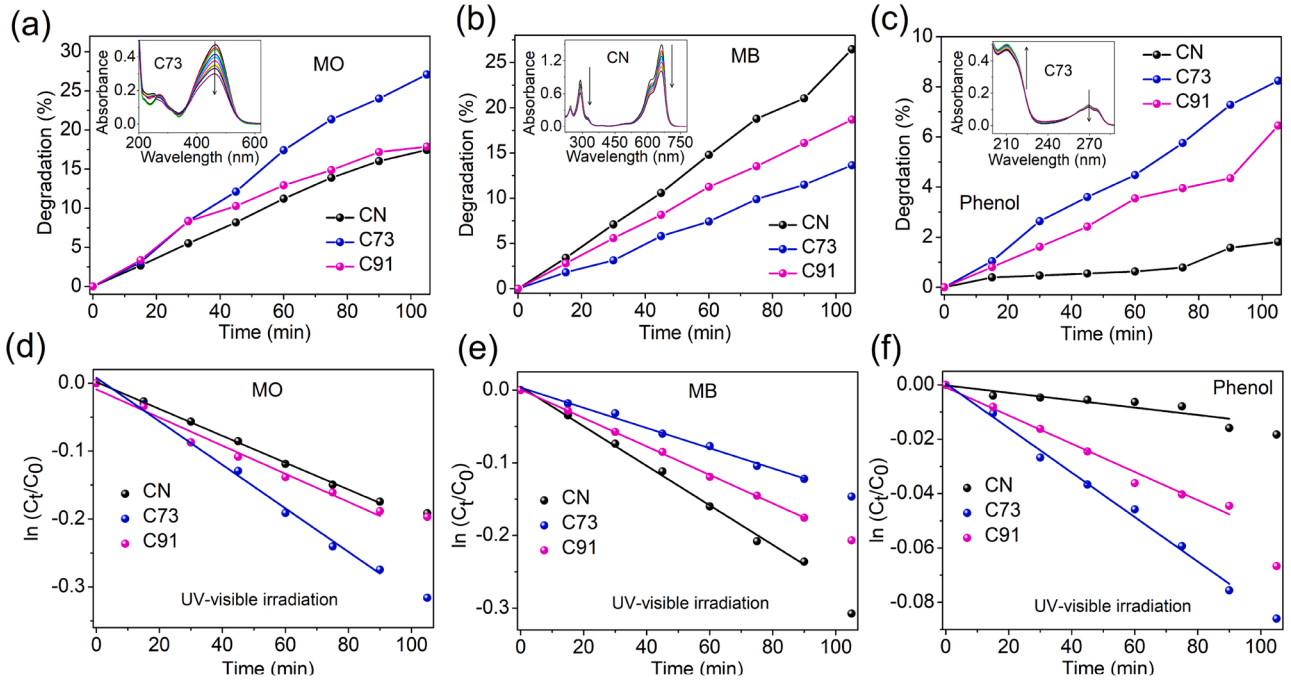

Fig. 15. Degradation curves and rate kinetics plot for (a, d) MO, (b, e) MB, (c, f) phenol degradation in the presence of pristine CN and bimetallic composites C73, C91 under UV–vis irradiation.

finally, the photocatalytic activity. The excitation wavelength also impacts the photocatalytic performance. While UV excitation improves the photocatalytic activity, UV–vis and green laser has a diminishing impact. Further, the oxidized Au^+ and Ag^+ states act as interfacial traps and impact the photocatalytic performance of the system. We have finally prepared a table that compares the photocatalysis (Table 3) of reported monometallic and bimetallic Ag, Au decorated systems with our present result. The table clearly shows that most photocatalytic works use a broadband solar light for photocatalysis [16,17,20,25,52–62]. On the other hand, we have provided selective excitations for a thorough understanding of excitonic and plasmonic phenomena on photocatalysis in our study.

4. Conclusion

The overall photocatalytic performance under UV, UV–vis, and green laser can be summed up in the following four points.

(1) XPS results confirm the presence of oxidized Ag^+ and Au^+ species along with metallic Au(0) and Ag(0) states in the bimetallic composite. These Ag^+ and Au^+ species act as interfacial trap centers and reduce the charge transfer efficiency of carriers from CN to the bimetals. Optical field simulation shows a reduced field intensity in the Ag-Au bimetal separation as compared to Ag-Ag or Au-Au separation.

(2) The promotion of *d-sp* interband transition in Au and Ag NPs and semiconductor excitation in CN contributes to enhanced photocatalytic performance under UV light.

(3) Under UV–vis light, FRET and PIRET occur in unison. However, the presence of Ag^+ and Au^+ species weaken the dipolar strength of PIRET. It leads to a dominance of FRET over PIRET, resulting in carrier transfer from the CN to the bimetals. The photoelectrons over the bimetals are reduced, contributing to fewer carriers for photocatalysis. A similar occurrence under green laser leads to a not so improved photocatalysis in the bimetallic composites compared to the pristine one.

(4) DFT and UPS spectra reveal that the Fermi electrons of Ag and Au NPs contribute more towards the VB of CN. Because of the nearest position, the hot electrons on the plasmonic metals recombine with the VB holes. It also contributes to a reduced photocatalysis under UV–vis and green laser illumination.

CRediT authorship contribution statement

Trishamoni Kashyap is responsible for the fabrication, result analysis, and writing of the manuscript.. **Sritam Biswas** and **Pabitra Nath** have contributed to optical field simulation and analysis. **Shahnaz Ahmed** and **Dhrubajyoti Kalita** have contributed localized structural study with density functional theory (DFT). **Biswajit Choudhury** is responsible for the overall planning and execution of the work and

Table 3
A comparison of photocatalytic activity of metal NPs decorated g-C_3N_4 with present report.

Material	Application	Light source	Result	Outcome	Reference
Ag/g-C_3N_4	Methyl orange (MO) degradation	Visible (300 W Xe lamp)	92 % degradation of MO in 60 min with Ag (5)/g-C_3N_4 under visible light	Enhanced activity with Ag loading over g-C_3N_4	16
Core-shell Ag@g-C_3N_4 nanocomposite	Photodegradation of MB dye	Visible (500 W Xe lamp)	2 times better activity in degradation with Ag@C_3N_4 than pristine C_3N_4	Highest activity with 0.5 wt% Ag@C_3N_4	17
Au-CNx composite	Degradation of methylene blue (MB), rhodamine B (RhB), methyl red (MR)	84 W UV, 130 W visible light, Natural sunlight	82 %, 90 %, 98 % RhB degradation in 120 min under UV, visible, sunlight; 81 %, 96 %, 90 % MB degradation in 120 min under UV, visible, sunlight; 82 %, 96%, 92% MR degradation in 150 min under UV, visible, sunlight	Enhanced activity for 40 wt% Au-CNx	20
Au-Ag/g-C_3N_4	Degradation of RhB dye	Visible(450 W Xe arc lamp)	90 % degradation in 240 min with 3%Au-Ag /g-C_3N_4	Enhanced activity for bimetallic Au-Ag/C_3N_4 than Au/C_3N_4, Ag/C_3N_4, pure C_3N_4	25
AuNP/g-C_3N_4 nanohybrids	Photodegradation of methyl orange (MO) dye	Visible (500 W Xe lamp)	92.6 % degradation with AuNP/g-C_3N_4 in 2.5 h	Enhanced activity with AuNP/g-C_3N_4	51
Ag/g-C_3N_4	Degradation of methyl orange (MO), methylene blue (MB), neutral dark yellow GL (NDY-GL)	Visible (500 W Xe lamp)	86 %,57 %,78 % degradation of MO, MB, NDY-GL in 120 min with Ag/g-C_3N_4	Better photocatalytic activity for Ag/g-C_3N_4	52
Ag/C_3N_4 nanocomposites	Degradation of rhodamine B (RhB) dye	Visible Xe lamp	Complete degradation of RhB in 60 min with Ag_{48}/C_3N_4	Best activity with 0.48 wt% Ag/C_3N_4	53
Mpg-C_3N_4/Ag composite	Photocatalytic methylene blue (MB) degradation	Visible (300 W Xe lamp)	60 % degradation of MB in 1 h with mpg-C_3N_4	Enhanced activity; best for 3 wt% Ag loaded Mpg-C_3N_4	54
Ag/g-C_3N_4 heterostructure	Photocatalytic degradation of rhodamine (RhB) dye	Visible (350 W Xe lamp)	85 % RhB degradation with Ag/D-C_3N_4 in 1 h	Enhanced activity for Ag/C_3N_4	55
Ag/g-$C_3N_{4.5}$ nanobelt	Degradation of rhodamine B (RhB) dye	500 W mercury lamp	95.7 % degradation in 75 min with Ag/g-$C_3N_{4.5}$	Enhanced activity for Ag/g-$C_3N_{4.5}$	56
Ag/porous g-C_3N_4	Photocatalytic degradation of Phenol	Visible (300 W Xe lamp)	Complete degradation in 210 min with 5 wt % Ag/g-C_3N_4	Enhanced photocatalytic activity of Ag/porous g-C_3N_4	57
Ag/g-C_3N_4	Degradation of Malachite green (MG) stain	UV (40 W)	80 % degradation within 100 min with Ag/C_3N_4	Higher photocatalytic activity for Ag/g-C_3N_4	58
Ag/g-C_3N_4	Degradation of rhodamine B (RhB) dye	Visible (500 kW Xe lamp)	98 % degradation in 50 min with 2 wt% Ag/g-C_3N_4	Enhanced activity for Ag/g-C_3N_4 nanosheets	59
Ag/g-C_3N_4 composite	Degradation of rhodamine B (RhB)	Visible (500 W Xe lamp)	100 % degradation of RhB in 100 min with 3 wt% Ag/g-C_3N_4	Enhanced activity with Ag/g-C_3N_4	60
Ag/CN-x (x = CN calcination time in h)	Photodegradation of methyl orange (MO)	Visible ($\lambda >$ 420)	98.6 % degradation efficiency within 2 h with Ag/CN-8	Enhanced activity for Ag/CN-x	61
Ag/Au bimetal decorated over g-C_3N_4	Degradation of RhB, MB, MO, phenol	UV 250 W, UV–vis 250 W lamp, green laser	53 % RhB degradation with bimetallic C91 under UV, 90 % degradation with C91 under UV–vis, 42 % degradation with C73 under Laser; in 105 min	Bimetallic composites show better activity under UV light; diminishing activity of the composites under UV–vis and green laser	Present report

writing of the manuscript.

Declaration of Competing Interest

The authors have no competing interests

Acknowledgments

BC would like to acknowledge Department of Science and Technology (DST, Govt. of India) for funding this research through DST INSPIRE Faculty award. BC would also like to thank Dr. Arup R. Pal, IASST, Guwahati for helping with photoconductivity measurement. The authors also acknowledge CSIR-NEIST, Jorhat for helping with XPS facility. The authors also acknowledge CIF, IASST Guwahati for the TEM facility.

Appendix A. Supplementary data

Supplementary material related to this article can be found, in the online version, at doi:https://doi.org/10.1016/j.apcatb.2021.120614.

References

[1] A. Fujishima, K. Honda, Electrochemical photolysis of water at a semiconductor electrode, Nature 238 (1972) 37–38, https://doi.org/10.1038/238037a0.
[2] H. Park, Y. Park, W. Kim, W. Choi, Surface modification of TiO_2 photocatalyst for environmental applications, J. Photochem. Photobiol. C Photochem. Rev. 15 (2013) 1–20, https://doi.org/10.1016/j.jphotochemrev.2012.10.001.
[3] B. Choudhury, S. Bayan, A. Choudhury, P. Chakraborty, Narrowing of band gap and effective charge carrier separation in oxygen deficient TiO_2 nanotubes with improved visible light photocatalytic activity, J. Colloid Interface Sci. 465 (2016) 1–10, https://doi.org/10.1016/j.jcis.2015.11.050.
[4] G. Duoerkun, Y. Zhang, Z. Shi, X. Shen, W. Cao, T. Liu, J. Liu, Q. Chen, L. Zhang, Construction of n-TiO_2/p-Ag_2O junction on carbon fiber cloth with Vis–NIR photoresponse as a filter-membrane-shaped photocatalyst, Adv. Fiber Mater. 2 (2020) 13–23, https://doi.org/10.1007/s42765-019-00025-8.
[5] S. Xiong, Y. Yu, P. Wang, M. Liu, S. Chen, X. Yin, L. Wang, H. Wang, Growth of AgBr/Ag_3PO_4 heterojunction on chitosan fibers for degrading organic pollutants, Adv. Fiber Mater. 2 (2020) 246–255, https://doi.org/10.1007/s42765-020-00042-y.
[6] Y. Sun, J.B. Mwandeje, L.M. Wangatia, F. Zabihi, J. Nedeljkovic, S. Yang, Enhanced photocatalytic performance of surface-modified TiO_2 nanofibers with rhodizonic acid, Adv. Fiber Mater. 2 (2020) 118–122, https://doi.org/10.1007/s42765-020-00037-9.
[7] X. Wang, K. Maeda, A. Thomas, K. Takanabe, G. Xin, J.M. Carlsoon, K. Domen, M. Antonietti, A metal-free polymeric photocatalyst for hydrogen production from water under visible light, Nat. Mater. 8 (2009) 76–80, https://doi.org/10.1038/nmat2317.
[8] S. Zhang, P. Gu, R. Ma, C. Luo, T. Wen, G. Zhao, W. Cheng, X. Wang, Recent developments in fabrication and structure regulation of visible-light driven g-C_3N_4-based photocatalysts towards water purification: a critical review, Catal. Today 335 (2019) 65–77, https://doi.org/10.1016/j.cattod.2018.09.013.
[9] B. Choudhury, P.K. Giri, Isotype heterostructure of bulk and nanosheets of graphitic carbon nitride for efficient visible light photodegradation of methylene blue, RSC Adv. 6 (2016) 24976–24984, https://doi.org/10.1039/C6RA00933F.
[10] C. Zhao, Z. Chen, R. Shi, X. Yang, T. Zhang, Recent advances in conjugated polymers for visible-light-driven water splitting, Adv. Mater. 32 (2020), 1907296, https://doi.org/10.1002/adma.201907296.
[11] C. Zhao, Z. Chen, J. Xu, Q. Liu, H. Xu, H. Tang, G. Li, Y. Jiang, F. Qu, Z. Lin, X. Yang, Probing supramolecular assembly and charge carrier dynamics toward enhanced photocatalytic hydrogen evolution in 2D graphitic carbon nitride nanosheets, Appl. Catal. B 256 (2019), 117867, https://doi.org/10.1016/j.apcatb.2019.117867.
[12] C. Zhao, C. Ding, C. Han, X. Yang, J. Xu, Lignin-incorporated supramolecular copolymerization yielding g-C_3N_4 nanoarchitectures for efficient photocatalytic hydrogen evolution, Sol. Rrl 5 (2021), https://doi.org/10.1002/solr.202000486, 2000486.
[13] C. Zhao, L. Tian, Z. Zou, Z. Chen, H. Tang, Q. Liu, Z. Lin, X. Yang, Revealing and accelerating interfacial charge carrier dynamics in Z-scheme heterojunctions for highly efficient photocatalytic oxygen evolution, Appl. Catal. B 268 (2020), 118445, https://doi.org/10.1016/j.apcatb.2019.118445.
[14] H. Xu, R. Xiao, J. Huang, Y. Jiang, C. Zhao, X. Yang, In situ construction of protonated g-C_3N_4/Ti_3C_2 MXene Schottky heterojunctions for efficient photocatalytic hydrogen production, Chinese J. Catal. 42 (2021) 107–114, https://doi.org/10.1016/S1872-2067(20)63559-8.
[15] T. Kashyap, S. Biswasi, A.R. Pal, B. Choudhury, Unraveling the catalytic and plasmonic roles of g-C_3N_4 supported Ag and Au nanoparticles under selective photoexcitation, ACS Sustainable Chem. Eng. 7 (2019) 19295–19302, https://doi.org/10.1021/acssuschemeng.9b05823.
[16] Y. Yang, Y. Guo, F. Liu, X. Yuan, Y. Guo, S. Zhang, W. Guo, M. Huo, Preparation and enhanced visible light photocatalytic activity of silver deposited graphitic carbon nitride plasmonic photocatalyst, Appl. Catal. B 142-143 (2013) 828–837, https://doi.org/10.1016/j.apcatb.2013.06.026.
[17] X. Bai, R. Zong, C. Li, D. Liu, Y. Liu, Y. Zhu, Enhancement of visible light photocatalytic activity via Ag@C_3N_4 core-shell plasmonic composite, Appl. Catal. B 147 (2014) 82–91, https://doi.org/10.1016/j.apcatb.2013.08.007.
[18] L. Xie, Z. Ai, M. Zhang, R. Sun, W. Zhao, Enhanced hydrogen evolution in the presence of plasmonic Au-photosensitized g-C_3N_4 with an extended absorption spectrum from 460 to 640 nm, PLoS One 11 (8) (2016), https://doi.org/10.1371/journal.pone.0161397 e0161397.
[19] Y. Guo, H. Jia, J. Yang, H. Yin, Z. Yang, J. Wang, B. Yang, Understanding the roles of plasmonic Au nanocrystal size, shape, aspect ratio and loading amount in Au/g-C_3N_4 hybrid nanostructures for photocatalytic hydrogen evolution, Phys. Chem. Chem. Phys. 20 (2018) 22296–22307, https://doi.org/10.1039/C8CP04241A.
[20] T. Bhowmik, M.K. Kundu, S. Barman, Ultra small gold nanoparticles-graphitic carbon nitride composite: an efficient catalyst for ultrafast reduction of 4 nitrophenol and removal of dyes from water, RSC Adv. 5 (2015) 38760–38773, https://doi.org/10.1039/C5RA04913J.
[21] S.M. Hosseini, M. Ghiaci, S.A. Kulinich, W. Wunderlich, H. Farrokhpour, M. Saraji, A. Shahvar, Au/Pd@g-C_3N_4 as an efficient photocatalyst for visible light oxidation of benzene to phenol: experimental and mechanistic study, J. Phy. Chem. C 122 (2018) 27477–42485, https://doi.org/10.1021/acs.jpcc.8b08788.
[22] C. Han, Y. Gao, S. Liu, L. Ge, N. Xiao, D. Dai, B. Xu, C. Chen, Facile synthesis of AuPd/g-C_3N_4 nanocomposite: an effective strategy to enhance photocatalytic hydrogen evolution activity, Int. J. Hydrogen Energy 42 (2017) 22765–22775, https://doi.org/10.1016/j.ijhydene.2017.07.154.
[23] W. Zou, L. Xu, Y. Pu, H. Cai, X. Wei, Y. Luo, L. Li, B. Gao, H. Wan, L. Dong, Advantageous interfacial effects of Ag/Pd/g-C_3N_4 for photocatalytic hydrogen evolution: electronic structure and H_2O dissociation, Chem. E. Journal 25 (2019) 5058–5064, https://doi.org/10.1002/chem.201806074.
[24] I. Majeed, U. Manzoor, F.K. Kanodarwala, M.A. Nadeem, E. Hussain, H. Ali, A. Badshah, J.A. Stride, M.A. Nadeem, Pd-Ag decorated g-C_3N_4 as an efficient photocatalyst for hydrogen production from water under solar light irradiation, Catal. Sci. Technol. 8 (2018) 1183–1193, https://doi.org/10.1039/C7CY02219K.
[25] M.A. Gondal, A.A. Adeseda, S.G. Rashid, A. Hameed, M. Aslam, I. Ismail, U. Baig, M.A. Dastageer, A.R. Al-Arfaj, A.U. Rehman, Facile synthesis, characterization and photocatalytic performance of Au-Ag alloy nanoparticles dispersed on graphitic carbon nitride under visible light irradiations, J. Mol. Catal. A Chem. 423 (2016) 114–125, https://doi.org/10.1016/j.molcata.2016.06.013.
[26] M.D. Vece, A.B. Laursen, L. Bech, C.N. Maden, M. Duchamp, R.V. Mateiu, S. Dahl, I. Chorkendorff, Quenching of TiO_2 photo catalysis by silver nanoparticles, J. Photochem. Photobiol. A: Chem. 230 (2012) 10–14, https://doi.org/10.1016/j.jphotochem.2011.12.025.
[27] E. Kowalska, M. Janczarek, L. Rosa, S. Juodkazis, B. Ohtani, Mono- and bi-metallic plasmonic photocatalysts for degradation of organic compounds under UV and visible light irradiation, Catal. Today 230 (2014) 131–137, https://doi.org/10.1016/j.cattod.2013.11.021.
[28] Z. Hai, N. Kolli, D.B. Uribe, P. Beaunier, M.J. Yacaman, J. Vigneron, A. Etcheberry, S. Sorgues, C.C. Justin, J. Chen, H. Remita, Modification of TiO_2 by bimetallic Au–Cu nanoparticles for wastewater treatment, J. Mater. Chem. A Mater. Energy Sustain. 1 (2013) 10829–10835, https://doi.org/10.1039/C3TA11684K.
[29] D. Gall, Electron mean free path in elemental metals, J. Appl. Phys. 119 (2016), 085101, https://doi.org/10.1063/1.4942216.
[30] J. Zhao, S.C. Nguyen, R. Ye, B. Ye, H. Weller, G.A. Somorjai, A.P. Alivisatos, F. D. Toste, A comparison of photocatalytic activities of gold nanoparticles following plasmonic and interband excitation and a strategy for harnessing interband hot carriers for solution phase photocatalysis, ACS Cent. Sci. 3 (2017) 482–488, https://doi.org/10.1021/acscentsci.7b00122.
[31] Y.-C. Huang, K.T. Arul, C.-L. Chen, J.-L. Chen, J. Chen, S. Shen, Y.-R. Lu, C.-H. Kuo, C.-L. Dong, W.-C. Chou, Electronic structures associated with enhanced photocatalytic activity in nanogap-engineered g-C_3N_4 /Ag@SiO_2 hybrid nanostructures, Appl. Surf. Sci. 514 (2020), 145907, https://doi.org/10.1016/j.apsusc.2020.145907.
[32] X. Li, Y. Yang, G. Zhou, S. Han, W. Wang, L. Zhang, W. Chen, C. Zou, S. Huang, The unusual effect of $AgNO_3$ on the growth of Au nanostructures and their catalytic performance, Nanoscale 5 (2013) 4976–4985, https://doi.org/10.1039/C3NR00603D.
[33] Y. Hui, R. Yan-yu, W. Tao, W. Chuang, Preparation and antibacterial activities of $Ag/Ag^{+}/Ag^{3+}$ nanoparticle composites made by pomegranate (Punica granatum) rind extract, Results Phys. 6 (2016) 299–304, https://doi.org/10.1016/j.rinp.2016.05.012.
[34] B. Choudhury, K.K. Paul, D. Sanyal, A. Hazarika, P.K. Giri, Evolution of nitrogen-related defects in graphitic carbon nitride nanosheets probed by positron annihilation and photoluminescence spectroscopy, J. Phys. Chem. C 122 (2018) 9209–9219, https://doi.org/10.1021/acs.jpcc.8b01388.
[35] S.W. Han, Y. Kim, K. Kim, Dodecanethiol-derivatized Au/Ag bimetallic nanoparticles: TEM, UV/VIS, XPS, and FTIR analysis, J. Colloid Interface Sci. 208 (1998) 272–278, https://doi.org/10.1006/jcis.1998.5812.
[36] L. Xu, D. Zhang, L. Ming, Y. Jiao, F. Chen, Synergistic effect of interfacial lattice Ag^{+} and Ag^{0} clusters in enhancing the photocatalytic performance of TiO_2, Phys. Chem. Chem. Phys. 16 (2014) 19358–19364, https://doi.org/10.1039/C4CP02658F.
[37] J.W. Yun, K.Y. Ryu, T.K. Nguyen, F. Ullah, Y.C. Park, Y.S. Kim, Tuning optical band gap by electrochemical reduction in TiO_2 nanorods for improving photocatalytic activities, RSC Adv. 7 (2017) 6202–6208, https://doi.org/10.1039/c6ra25274e.

[38] T.V.M. Sreekanth, P.C. Nagajyothi, G.R. Dillip, Y.R. Lee, Determination of band alignment in the synergistic catalyst of electronic structure-modified graphitic carbon nitride-integrated ceria quantum-dot heterojunctions for rapid degradation of organic pollutants, J. Phys. Chem. C 121 (2017) 25229–25242, https://doi.org/10.1021/acs.jpcc.7b08568.
[39] Analysis Features, UV Photoelectron Spectroscopy, Thermoscientific XPS, 2021 (accessed on 8 April, 2021), https://xpssimplified.com/UPS.php.
[40] S. Ahmed, D.J. Kalita, Charge transport in isoindigo-dithiophenepyrrole based D-A type oligomers: a DFT/TD-DFT study for the fabrication of fullerene-free organic solar cells, J. Chem. Phys. 149 (2018), 234906, https://doi.org/10.1063/1.5055306.
[41] S. Ahmed, B.C. Mushahary, D.J. Kalita, Rational design of bay-annulated indigo (BAI)-based oligomers for bulk heterojunction organic solar cells: a density functional theory (DFT) study, ACS Omega 5 (2020) 8321–8333, https://doi.org/10.1021/acsomega.0c00784.
[42] F. Manzoor, J. Iqbal, Z. Zara, B. Eliasson, M.S. Mahr, K. Ayub, Theoretical calculations of the optical and electronic properties of dithienosilole and dithiophene-based donor materials for organic solar cells, Chemistry Select 3 (2018) 1593–1601, https://doi.org/10.1002/slct.201703086.
[43] T. Kashyap, P.J. Boruah, H. Bailung, D. Sanyal, B. Choudhury, Simultaneous layer exfoliation and defect activation in g-C3N4 nanosheets in air-water interfacial plasma: spectroscopic defects probing with tailored optical properties, Nanoscale Adv. 3 (2021) 3260–3271, https://doi.org/10.1039/D1NA00098E.
[44] N.T. Khoa, S.W. Kim, D.-H. Yoo, S. Cho, E.J. Kim, S.H. Hahn, Fabrication of Au/graphene-wrapped ZnO-nanoparticle-assembled hollow spheres with effective photoinduced charge transfer for photocatalysis, ACS Appl. Mater. Interfaces 7 (2015) 3524–3531, https://doi.org/10.1021/acsami.5b00152.
[45] K.K. Paul, P.K. Giri, H. Sugimoto, M. Fujii, B. Choudhury, Evidence for plasmonic hot electron injection induced superior visible light photocatalysis by g-C_3N_4 nanosheets decorated with Ag–TiO_2(B) and Au–TiO_2(B) nanorods, Sol. Energy Mater. Sol. Cells 201 (2019), 110053, https://doi.org/10.1016/j.solmat.2019.110053.
[46] C. Lee, Y. Park, J.Y. Park, Hot electrons generated by intraband and interband transition detected using a plasmonic Cu/TiO_2nanodiode, RSC Adv. 9 (2019) 18371–18376, https://doi.org/10.1039/C9RA02601K.
[47] L.J. Brennan, F.P. Milton, A.S. Salmeron, H. Zhang, A.O. Govorov, A.V. Fedorov, Y. K. Gun'ko, Hot plasmonic electrons for generation of enhanced photocurrent in gold-TiO_2 nanocomposites, Nanoscale Res. Lett. 10 (38) (2015) 1–12, https://doi.org/10.1186/s11671-014-0710-5.
[48] P.F. Wang, Y. Liu, J. Yin, W. Ma, Z. Dong, W. Zhang, J.L. Zhu, J.L. Sun, A tunable positive and negative photoconductive photodetector based on a gold/graphene/p-type silicon heterojunction, J. Mater. Chem. C 7 (2019) 887–896, https://doi.org/10.1039/C8TC05404E.
[49] F. Binkowski, T. Wu, P. Lalanne, S. Burger, A.O. Govorov, Hot Electron generation through near-field excitation of plasmonic nanoresonators, ACS Photonics 8 (2021) 1243–1250, https://doi.org/10.1021/acsphotonics.1c00231.
[50] A. Zielińska-Jurek, E. Kowalska, J.W. Sobczak, W. Lisowski, B. Ohtani, A. Zaleska, Preparation and characterization of monometallic (Au) and bimetallic (Ag/Au) modified-titania photocatalysts activated by visible light, Appl. Catal. B 101 (2011) 504–514, https://doi.org/10.1016/j.apcatb.2010.10.022.
[51] J. Li, S.K. Cushing, F. Meng, T.R. Senty, A.D. Bristow, N. Wu, Plasmon induced resonance energy transfer for solar energy conversion, Nat. Photonics 9 (2015) 601–607, https://doi.org/10.1038/nphoton.2015.142.
[52] N. Cheng, J. Tian, Q. Liu, C. Ge, A.H. Qusti, A.M. Asiri, A.O. Al-Youbi, X. Sun, Au-nanoparticle-loaded graphitic Carbon Nitride nanosheets: green photocatalytic synthesis and application toward the degradation of organic pollutants, ACS Appl. Mater. Interfaces 5 (2013) 6815–6819, https://doi.org/10.1021/am401802r.
[53] Y. Fu, T. Huang, L. Zhang, J. Zhu, Xin Wang, Ag/g-C_3N_4 catalyst with superior catalytic performance for the degradation of dyes: a borohydride-generated superoxide radical approach, Nanoscale 7 (2015) 13723, https://doi.org/10.1039/C5NR03260A.
[54] K. Tian, W.-J. Liu, H. Jiang, Comparative Investigation on photoreactivity and mechanism of biogenic and chemosythetic Ag/C3N_4 composites under visible light irradiation, ACS Sustain. Chem. Eng. 3 (2015) 269–276, https://doi.org/10.1021/sc500646a.
[55] Q. He, F. Zhou, S. Zhan, Y. Yang, Y. Liu, Y. Tian, N. Huang, Enhancement of photocatalytic and photoelectrocatalytic activity of Ag modified Mpg-C_3N_4 composites, Appl. Surf. Sci. 391 (2017) 423–431, https://doi.org/10.1016/j.apsusc.2016.07.005.
[56] C. Min, C. Shen, R. Li, Y. Li, J. Qin, X. Yang, In-situ fabrication of Ag/g-C_3N_4 composite materials with improved photocatalytic activity by coordination-driven assembly of precursors, Ceram. Int. 42 (2016) 5575–5581, https://doi.org/10.1016/j.ceramint.2015.12.042.
[57] R. Lei, J. Jian, Z. Zhang, B. Song, R. Wu, Bifunctional Ag/$C_3N_{4.5}$ composite nanobelts for photocatalysis and antibacterium, Nanotechnology 27 (2016), 395603, https://doi.org/10.1088/0957-4484/27/39/395603.
[58] Z. Han, N. Wang, H. Fan, S. Ai, Ag nanoparticles loaded on porous graphitic carbon nitride with enhanced photocatalytic activity for degradation of phenol, Solid State Sci. 65 (2017) 110–115, https://doi.org/10.1016/j.solidstatesciences.2017.01.010.
[59] P.C. Nagajyothi, M. Pandurangan, S.V.P. Vattikuti, C.O. Tettey, T.V.M. Sreekanth, J. Shim, Enhanced photocatalytic activity of Ag/g-C_3N_4 composite, Sep. Purif. Technol. 188 (2017) 228–237, https://doi.org/10.1016/j.seppur.2017.07.026.
[60] J. Jin, Q. Liang, C. Ding, Z. Li, S. Xu, Simultaneous synthesis-immobilization of Ag nanoparticles functionalized 2D g-C_3N_4 nanosheets with improved photocatalytic activity, J. Alloys. Compd. 691 (2017) 763–771, https://doi.org/10.1016/j.jallcom.2016.08.302.
[61] K. Qi, Y. Li, Y. Xie, S.-y. Liu, K. Zheng, Z. Chen, R. Wang, Ag loading enhanced photocatalytic activity of g-C_3N_4 porous nanosheets for decomposition of organic pollutants, Front. Chem. 7 (91) (2019) 1–9, https://doi.org/10.3389/fchem.2019.00091.
[62] R. Liu, W. Yang, G. He, W. Zheng, M. Li, W. Tao, M. Tian, Ag-Modified g-C_3N_4 prepared by a one-Step calcination method for enhanced catalytic efficiency and stability, ACS Omega 5 (2020) 19615–19624, https://doi.org/10.1021/acsomega.0c02161.